USC–SIPI REPORT #211

Error Bounds for EEG and MEG Dipole Source Localization

by

John C. Mosher, Michael E. Spencer, Richard M. Leahy, and Paul S. Lewis

July 1992

Signal and Image Processing Institute
UNIVERSITY OF SOUTHERN CALIFORNIA
Department of Electrical Engineering-Building
University Park/MC-2564
Los Angeles, CA 90089 U.S.A.

Error Bounds for EEG and MEG Dipole Source Localization[1]

John C. Mosher,[*+#] Michael E. Spencer,[*#] Richard M. Leahy,[*] and Paul S. Lewis[+]
[*]Signal and Image Processing Institute, University of Southern California, Los Angeles, CA 90089-2564
[+]Los Alamos National Laboratory, MEE-3, Los Alamos, NM 87545
[#]TRW, Inc., One Space Park, Redondo Beach, CA 90278.

Abstract: General formulas for computing the lower bound in both localization and moment error for electroencephalographic (EEG) or magnetoencephalographic (MEG) current dipole models with arbitrary sensor array geometry are presented. Specific EEG and MEG formulas are presented for the case of multiple dipoles in a four spherical shell head model. Localization error bounds are presented for both EEG and MEG for several different sensor configurations. Graphical error contours are presented for 127 sensors covering the upper hemisphere, for both 37 sensors and 127 sensors covering a smaller region, and for the standard Ten-Twenty EEG sensor arrangement. One and two dipole cases are examined for all possible dipole orientations and locations within a head quadrant. The results show a strong dependence on absolute dipole location and orientation. Fusion of EEG and MEG measurements into a combined model is shown to reduce the lower bound. A Monte-Carlo simulation is performed to check the tightness of the bounds for a selected case. The simple head model, the white and relatively low power noise, and the few relatively strong dipoles were all selected in this study as optimistic conditions in order to establish possibly fundamental resolution limits for any localization effort. Results under these favorable assumptions show comparable resolutions between EEG and MEG, but accuracy for a single dipole in either case appears limited to several millimeters for a single time slice. The lower bounds markedly increase with just two dipoles. Observations are given to support the need for full spatio-temporal modeling to improve these lower bounds. All simulation results presented are easily scaled to other instances of noise power and dipole intensity.

Key Words: Spatio-temporal source modeling, EEG, MEG, dipole source localization error, dipole moment error.

---

1. This work was supported by the Los Alamos National Laboratory, operated by the University of California for the United States Department of Energy under contract W-7405-ENG-36, by the TRW Doctoral Fellowship Program, and by the Kaprielian Innovative Research Fund at the University of Southern California.
Correspondence to: Dr. R. Leahy, Signal & Image Processing Institute, University of Southern California, Los Angeles, CA 90089-2564.

1.0 Introduction

Electroencephalograms (EEG) and magnetoencephalograms (MEG) are non-invasive methods of studying the functional activity of the human brain with millisecond temporal resolution. Much of the work in EEG and MEG in the last few decades has focused on estimating the properties of the internal sources of the fields from the external measurements (Snyder, 1991). The most straightforward model for describing the surface evoked potential or evoked magnetic field is the single equivalent current dipole. In (Mosher et al., 1992), we review the many variations of this dipole model and its extensions to multiple dipoles and time epochs. Each of the models, both in EEG and MEG, contains a transfer function or lead field model to relate the dipole's intensity, orientation, and location to the externally measured fields. The general inverse problem is to find the three location parameters and three moment parameters that comprise the unknown parameters for each dipole.

The simplest head model in use is a set of homogeneous spherical shells, for which the MEG model is straightforward and the EEG model still tractable, except with more parameter assumptions. Although a dipole comprises six parameters, the focus in most research to date has been on the accuracy of determining the three location parameters. Early studies almost immediately began comparing the relative localizing ability of EEG and MEG (Cuffin and Cohen, 1979, Cohen and Cuffin, 1983). In (Stok, 1987), the various model parameters were varied to determine which had the greatest impact in accuracy. In (Cuffin, 1990 and Cuffin, 1991), the head shape and sphere models are examined for their accuracy impacts. In (Cuffin, 1986), variations of noise and measurement errors were explored for several array configurations. In (Kaufman et al., 1991), the dipole source is expanded to a larger spatial extent to test the dipole assumption in cortical folds for both EEG and MEG models. In (Achim et al., 1991, Baumgartner et al., 1991), the spatio-temporal model was examined for its effects in improving location accuracies.

Direct analysis of the localization error is complicated by the location parameters, sensitivity to the moment orientation, moment intensity, background noise power, the orientation and spatial extent of the sensors, and the absolute position of the dipole. Consequently, in most of the studies and comparisons listed above, the cases were either restricted to specialized dipole locations and/or sensor positions. The error results were generally established by experimental data or by Monte Carlo analysis. More recently,

dipoles implanted in patients have been used as an attempt to determine localization errors in MEG (Balish et al., 1991) and as a comparison between localization errors in EEG and MEG (Cohen et al., 1990). The results of (Cohen et al., 1990) have particularly lead to recent controversy, with the study criticized on methodological grounds in (Hari et al., 1991, Williamson, 1991). In (Therapeutics and Technology Assessment, 1992) and (Anogianakis et al., 1992), the call is for a careful consideration of the absolute accuracies of either modality under conditions fair to both. As noted in (Cohen and Cuffin, 1983) and repeated in (Anogianakis et al., 1992), EEG and MEG provide complementary data, and the use of both can contribute to overall improved accuracy.

Here we present an analysis of dipole localization error for MEG and EEG that is based on the well-known Cramer-Rao Lower Bound (CRLB). The CRLB provides a lower bound on the variance of *any* unbiased estimator of the location and other model parameters. By deriving a closed form expression for the bound, we are able to compute it efficiently for a much wider range of conditions than can studies based on Monte-Carlo simulations or experimental data. The bounds are useful only if they are relatively tight (i.e. they are not overly optimistic compared to the true localization error variances), and if the estimators that are employed have relatively small biases. To demonstrate the usefulness of the bounds, we present a Monte Carlo simulation that indicates that the CRLBs in most cases give reasonably accurate predictions of actual localization error variances. Preliminary results of this analysis are presented in (Mosher et al., 1990b).

We note that there are important limitations to this analysis, primarily due to the fact that the CRLB holds only under the assumption that the model is correct. The bounds give no insight into the effect of modeling error on localization accuracy. Nevertheless, in many of the cases shown below, the CRLB gives surprisingly large lower bounds, even under fairly optimistic assumptions. Since modeling errors tend to degrade rather than improve performance, these results indicate that the accuracy of dipole localization based on single time epochs is often limited by the inherent ill-posedness of the problem. The models used here are some of the simplest in use. In general, more complicated models will be more prone to modeling errors and/or have more parameters to estimate. Consequently the bounds presented here may pose fundamental limits on EEG and MEG localization performance.

In this paper, we present the Cramer-Rao lower bound for the general spatio-temporal model for an arbitrary number of sensors, an arbitrary number of time instances, and an arbitrary number of dipoles with arbitrary moments. We then present formulas for the

dipoles in a four shell sphere model for both the EEG and MEG case. These formulas are used in the subsequent sections to examine lower bound on errors for several different array and dipole configurations. The localization error bounds are computed for one and two dipoles located in a plane in the upper hemisphere of the head. For each location, a search is performed over all possible dipole orientations for the best and worst results, as well as the average localization error bounds. Graphical error contours are displayed for a quadrant in the upper head hemisphere, providing rapid assessment and comparison of the two modalities.

The emphasis throughout this paper is to present optimistic operating conditions with perfect models, many sensors, and low noise power, so that we may establish if the corresponding lower bounds indicate the potentials for good dipole resolution. The use of identical sensor patterns allows in each case a cautious, but direct comparison of the differences in MEG and EEG source localization ability.

2.0 Forward Models

In this section we first discuss the general spatio-temporal model common to both EEG and MEG. We then present EEG and MEG version of the "dipole in a sphere" model, where sources are represented by current dipoles, and the head is modeled as a four concentric shell sphere. This model illustrates how we adapt a specific EEG or MEG model to the general electromagnetic model, which is in turn used to determine the Cramer-Rao lower bounds.

2.1 The General Model

By the superposition of electromagnetic sources, we can always separate the intensity of the sources as a linear term, whether we are considering these simple EEG and MEG spherical models or any other combination of head and source model. The vector of measured samples at time j can be modeled as

$$\underline{A}(j) = \left[\mathbf{G}(\grave{\imath}_1)\ \mathbf{G}(\grave{\imath}_2)\ \ldots\ \mathbf{G}(\grave{\imath}_p)\right]\begin{bmatrix}\grave{q}_1\\ \grave{q}_2\\ \ldots\\ \grave{q}_p\end{bmatrix} = \mathbf{G}(\mathbf{l})\underline{g}(j), \qquad \text{(EQ 1)}$$

where $\underline{A}(j)$ represents the general column vector of surface potential or magnetic field measurements, or a combination of both. Column vectors $\underline{l}$ and $\underline{q}$ are both concatenations of the parameters for p dipoles, $\underline{l} = \left[\vec{l}_1, \ldots, \vec{l}_p\right]^T$ and $\underline{q} = \left[\vec{q}_1, \ldots, \vec{q}_p\right]^T$. The vector $\vec{l}_i$ represents the three-dimensional location of the ith current dipole, and $\vec{q}_i$ represents the corresponding three-dimensional dipole moment. $G(\vec{l}_i)$ represents the "gain transfer" matrix for the ith dipole, which relates the dipoles' moments to the vector of measurements and has a non-linear dependence on the dipole locations.

For n time slices, we can extend this model by assuming the dipole locations are fixed, but allowing the dipole moments to vary with time:

$$\mathbf{A} = [\underline{A}(1), \ldots, \underline{A}(n)] = \mathbf{G}(\underline{l})\,[\underline{q}(1), \ldots, \underline{q}(n)] = \mathbf{G}(\underline{l})\mathbf{Q} \quad . \qquad \text{(EQ 2)}$$

We could also fix the dipole orientation over the time interval and factor out just the magnitude as a function of time, but for simplicity in this work we do not apply this restriction. In (Mosher et al., 1990, 1992), details are presented which expand this representation for the "unconstrained", "rotating", and "fixed" orientation dipole models.

2.2 Four Concentric Sphere Model for EEG

The EEG dipole model is the more complex of the two models, and assumptions must be made for the conductivities and shell thicknesses. The earliest models were for the dipole in a single homogeneous sphere (Wilson and Bayley, 1950), which led to a closed form solution (Brody et al.1973); however, this single sphere model is too simplistic because it does not model the relatively high resistivity of the skull layer. A three concentric sphere model that includes cerebrospinal fluid and skull layers was derived by (Arthur and Geselowitz, 1970). (Ary et al., 1981) state the one and three sphere models, but they are missing a $1/(R^2)$ scaling factor on the surface potential. The four sphere model, which also accounts for the scalp layer, is derived by (Cuffin and Cohen, 1979). Other models recently published include the three eccentric sphere model (Cuffin, 1991) and the four sphere anisotropic model (Zhou and van Oosterom1992).

In this paper we use the four concentric sphere model. For a single dipole model at point $\vec{l}$, each element in (1) of the column vector of surface potential measurements represents the voltage at a single surface point $\vec{p}$ and is expressed as the inner product of a (3 x 1) gain vector $\vec{g}_v$and the (3 x 1) dipole moment vector $\vec{q}$:

$$V(\vec{p}) = \vec{g}_V^T(\vec{l}, \vec{p})\vec{q} \qquad \text{(EQ 3)}$$

where for clarity we show the dependence of the gain vector on both the dipole location and sensor position. The gain matrix $\mathbf{G}(\vec{l})$ for a single dipole is the concatenation of the gain vectors for all sensor positions $\vec{p}$.

Fig. 1 shows the coordinate system used for the basic EEG formulas. For a dipole on the z-axis, the potential on the surface of the four sphere model referenced to infinity is given by (Cuffin and Cohen, 1979). Other dipole locations are found by applying rotation transformations to the basic formulas. We can express the four sphere model in rotated Cartesian coordinates for arbitrary dipole position as

$$\hat{g}_V(\vec{l}, \vec{p}) = \sum_{n=1}^{\infty} w(n) \left(\frac{\vec{l}}{R}\right)^{n-1} [\hat{a}_{x'} P_n^1(\cos\theta') \cos\phi' + \hat{a}_{y'} P_n^1(\cos\theta') \sin\phi' + \hat{a}_{z'} n P_n(\cos\theta')] \qquad \text{(EQ 4)}$$

where

$P_n(.)$	=	Legendre polynomial of order n
$P_n^1(.)$	=	Associated Legendre polynomial
R	=	outside radius of head sphere (in m)
$\hat{a}_{x'}, \hat{a}_{y'}, \hat{a}_{z'}$	=	rotated coordinate axes relative to dipole location
θ', ϕ'	=	angle between rotated axes and sensor location (Fig. 1)

The weighting function w(n) in (4) is given by

$$w(n) = \left(\frac{1}{4\pi\sigma_4 R^2}\right) \frac{(2n+1)^4 (cd)^{2n+1}}{n\Gamma(n)} \qquad \left(\frac{V}{Am}\right) \qquad \text{(EQ 5)}$$

where

$$\begin{aligned} \Gamma(n) = {} & d^{2n+1} \{ b^{2n+1} n (k_1 - 1)(k_2 - 1)(n+1) + c^{2n+1} (k_1 n + n + 1)(k_2 n + n + 1) \} \\ & \cdot \{ (k_3 n + n + 1) + (n+1)(k_3 - 1) d^{2n+1} \} \\ & + (n+1) c^{2n+1} \{ b^{2n+1} (k_1 - 1)(k_2 n + k_2 + n) + c^{2n+1} (k_1 n + n + 1)(k_2 - 1) \} \\ & \cdot \{ n(k_3 - 1) + (k_3 n + k_3 + n) d^{2n+1} \} \end{aligned} \qquad \text{(EQ 6)}$$

$$k_1 = \frac{\gamma_1}{\gamma_2}, \quad k_2 = \frac{\gamma_2}{\gamma_3}, \quad k_3 = \frac{\gamma_3}{\gamma_4} \qquad \text{(EQ 7)}$$

and γ_1, γ_2, γ_3, γ_4 are the conductivities of brain, CFC, skull, and scalp, respectively, and b, c, d are the inner sphere radii normalized to the outer head sphere radius. Fig. 2 shows the four spheres with their respective radii and conductivities. Overlaid on the spheres are the sensor locations for the 37 channel pattern, one of the sensor arrays analyzed in this paper.

This model explicitly shows that the voltage has a nonlinear dependence on the dipole and electrode locations and a linear dependence on the dipole moment. The conductivities and radii shown were drawn from (Cuffin and Cohen, 1979). We note that the relatively thin skull thickness of 4 mm in this case gives favorable values for dipole localization; thicker skulls will produce higher error bounds. (Stoke, 1978), for example, uses a skull thickness of 6 mm.

2.3 Biot-Savart Law for MEG

Compared to its EEG counterpart, the MEG model for the dipole in a sphere with radially oriented sensors is quite simple. Radially oriented dipoles produce no magnetic field outside the concentric conducting spheres, regardless of the number of spheres we consider. Return volume currents produce no external magnetic fields in the radial direction. (Sarvas, 1987) provides a thorough derivation of the general MEG formulas, then presents the simplifications that result for the case of the spherically symmetric head model with radially oriented sensors.

For radially oriented sensors, the measured field is a relatively simple function of just the tangential components of the dipole moments. As noted by (Ilmoniemi et al., 1985, Sarvas, 1987), the non-radial sensor orientations record magnetic fields that are also functions of only the tangential dipole moments, but the partials with respect to all of the parameters are not as simple as for the radial sensors. The restriction to the radial direction for sensor orientation is a common one; however, the analysis presented here makes it possible to study directly the question posed by (Ilmoniemi et al., 1985) as to the improvement gained for other sensor orientations.

We restrict ourselves to the radially oriented sensors, primarily for its simplicity in presentation. This model has been extensively reviewed and published in the recent literature, and we present here only a brief summary for completeness in relating this model to the terminology used here. The radially oriented MEG sensor coil is assumed to make a point measurement of the radial magnetic field. This scalar radial magnetic field $B(\vec{p})$ due to

a dipole located at $\vec{l}$ can be expressed as the inner product of gain vector $\vec{g}_B$ and the dipole moment $\vec{q}$,

$$B(\vec{p}) = \vec{g}_B^T(\vec{l}, \vec{p})\vec{q}, \qquad \text{(EQ 8)}$$

for sensor coil location $\vec{p}$. For the case of the spherical head model and radial sensor measurements, this gain vector is a special case of the Biot-Savart law and can be expressed as

$$\vec{g}_B(\vec{l}, \vec{p}) = \left(\frac{\mu_0}{4\pi}\right) \frac{(\hat{r} \times \vec{l})}{\|\vec{p} - \vec{l}\|^3} \qquad \text{(EQ 9)}$$

where the coordinate system is assumed to be head centered and

$\hat{r}$ = unit radial orientation of the sensor coil, $\vec{p}/\|\vec{p}\|$

μ_0 = permeability of free space = $4\pi \times 10^{-7}$ (Vs/(Am))

and " $\times$ " denotes the vector cross product. The MEG gain matrix $G(\vec{l})$ for a single dipole is the concatenation of all gain vectors for all sensor locations.

3.0 Cramer-Rao Lower Error Bound

The Cramer-Rao lower bound (CRLB) (e.g., Sorenson, 1985) is an important result in estimation theory that establishes a lower bound on the variance of any unbiased estimator of a set of unknown parameters. In order to determine the bound, a joint probability density function for the data is required. While the existence of an unbiased estimator that attains the bound is not guaranteed, we can use the bound to establish fundamental lower limits on the accuracy with which the parameters may be estimated. In the application of the CRLB to dipole localization, we can use this result to determine, under certain modeling assumptions, minimum mean squared localization errors for dipolar sources. For these bounds to be meaningful in this application, we need to show that (a) the estimators we use are effectively unbiased, and (b) the bounds are relatively tight, i.e. that the lower bound on the variance is close to the true attainable variance with a given estimator. To investigate the utility of the CRLB, we performed Monte-Carlo studies using non-linear least-squares for localization. The results of this study are reported in Section 4.0.

3.1 Fisher Information Matrix

Consider a set of data **F**, which we model as $\mathbf{F} = \mathbf{G}(\mathbf{l})\mathbf{Q} + \mathbf{N}$, where **N** is the unknown noise and $\mathbf{G}(\mathbf{l})\mathbf{Q}$ is the noiseless deterministic data. We assume that the locations $\mathbf{l}$ and the orientations and magnitudes **Q** of the dipole moments are unknown. We assume that the noise **N** is zero-mean, spatially and temporally white, normally distributed and has an unknown variance v. For convenience, we group these parameters into one vector ψ,

$$\psi = [v, \underline{q}(1)^T, \ldots, \underline{q}(n)^T, \underline{l}_1^T, \ldots, \underline{l}_p^T]^T, \qquad \text{(EQ 10)}$$

where each moment vector at each time instance j is the concatenation of the individual moments for each dipole,

$$\underline{q}(j)^T = [\underline{\hat{q}}_1^T(j), \ldots, \underline{\hat{q}}_p^T(j)] . \qquad \text{(EQ 11)}$$

Cramer-Rao Inequality Theorem: *Let $\hat{\psi}$ be any unbiased estimate of the deterministic parameters in* $\mathbf{F} = \mathbf{G}(\mathbf{l})\mathbf{Q} + \mathbf{N}$. *Then the covariance matrix C of the errors between the actual and estimated parameters is bounded from below by the inverse of* **J**

$$\mathbf{C} = \mathbf{E}\{(\psi - \hat{\psi})(\psi - \hat{\psi})^T\} \geq \mathbf{J}^{-1} \qquad \text{(EQ 12)}$$

where **J** *is the Fisher Information Matrix,*

$$\mathbf{J} = \mathbf{E}\left\{\left[\frac{\partial}{\partial \psi}\log\ p(\mathbf{F}|\psi)\right]\left[\frac{\partial}{\partial \psi}\log\ p(\mathbf{F}|\psi)\right]^T\right\}, \qquad \text{(EQ 13)}$$

E{ } denotes the expected value or mean of the enclosed term and $p(\mathbf{F}|\psi)$ *the probability density function for the data with parameters* ψ.

See (Sorenson, 1985) for a proof of this result. The inequality in (12) states that the difference matrix $(\mathbf{C} - \mathbf{J}^{-1})$ is positive semi-definite, and as a consequence, the variance of each parameter ψ_i is individually bounded by the corresponding diagonal element in $\mathbf{J}^{-1}$. Under the assumption that the noise is spatially and temporally white and normally distributed, an analytic expression for (12) is possible. In the Appendix, we derive this result for the case of m sensors, n time instances, and p dipoles in a general form that is applicable to both EEG and MEG data.

The Fisher Information Matrix and its inverse in the Appendix give insight into how each parameter affects the estimate of the other parameters. Repeating (23) from the

Appendix, for m sensors, n time slices, and variance ν, and with $\mathbf{G}$, Δ and Γ defined in the Appendix, the Fisher Information Matrix is

$$\mathbf{J} = \frac{1}{\nu}\begin{bmatrix} \left[\frac{mn}{2\nu}\right] & 0 & 0 \\ 0 & \left[\mathbf{I}_n \otimes \mathbf{G}^T\mathbf{G} \;\; \Delta\right] \\ 0 & \left[\Delta^T \;\; \Gamma\right] \end{bmatrix}. \qquad \text{(EQ 14)}$$

The upper left diagonal term in $\mathbf{J}$, $(mn)/(2\nu)$, represents the information for the estimate of the noise power. The other entries in the first column and first row represent the cross-information between the noise power and the other parameters of our model, namely the moments and locations of the dipoles; these off-diagonal elements are zero. The CRLB requires inversion of this matrix, and these zeros allow us to partition the matrix into two separate submatrices and invert them separately. Thus the parameters in one submatrix cannot affect the parameters in the other. This indicates that knowledge of the noise power does *not* affect the lower bounds of the moments and location, and vice versa. Thus whether or not we assume we know the noise power does not impact our lower bounds for the other parameters.

The information for the moments and location is represented here by the lower right submatrix in (14). The cross-information between the moments and the locations is represented by the off-diagonal term Δ. If we assumed perfect knowledge of the moments, then the CRLB of the locations would reduce to the first bracketed term in (25). Similarly, if the locations are perfectly known, the CRLB for the moments would reduce to the first bracketed term in (27). In the general dipole localization problem, we know neither the moment nor the location, and the second term in each of these CRLB equations shows that we cannot simply ignore the cross-information term Δ. This cross coupling will always increase the error lower bounds, except for the rather specialized case of $\mathbf{P}_G^{\perp}\mathbf{D} = \mathbf{D}$, i.e., where the partials matrix is completely orthogonal to the gain matrix. Thus consideration of the estimation of both the moment and the location is critical to better lower bound accuracy.

3.2 Location Error Lower Bounds

Equations (24), (26), and (27) in the Appendix are for the general multiple dipole spatio-temporal model and express the lower bound for the variance, the dipole location, and the dipole moment. Our approach in this paper is to focus on the variance of the dipole

location error, since much MEG and EEG work emphasizes the ability or inability of the different modalities to locate the source of neural activity. In order to gain insight into the utility of the formulas and establish some basic lower bounds, we simplify the studies to the single time slice case and to the case of multiple dipole sources of equal scalar intensity Q. In this case, the scalar Q factors out and can be grouped with the variance of the noise. Simplifying (26) from the Appendix,

$$\text{CRLB}(\mathbf{I}) = \frac{\nu}{Q^2}\left[(\mathbf{D}\hat{\mathbf{X}})^T \mathbf{P}_G^{\perp} (\mathbf{D}\hat{\mathbf{X}}) \right]^{-1}. \qquad \text{(EQ 15)}$$

where CRLB( ) denotes the Cramer-Rao lower bound on the error covariance matrix of the enclosed vector, and ν is the variance of the additive Gaussian noise. The matrices $\mathbf{D}$, $\hat{\mathbf{X}}$, and $\mathbf{P}_G^{\perp}$ are explicitly defined in the Appendix, but broadly speaking, $\mathbf{D}$ represents the matrix of partial derivatives of the gain transformation with respect to the locations, $\hat{\mathbf{X}}$ represents the moment orientations scaled to unity, and $\mathbf{P}_G^{\perp}$ is a projection operator onto the orthogonal complement of the column space of the gain matrix $\mathbf{G}$. Equation (15) illustrates how the dipole intensity and the noise variance can be lumped into a single scalar ratio of the two values, ν/Q^2, and that the moment orientation can be isolated into a single term $\hat{\mathbf{X}}$. We can therefore easily scale our results for any desired noise power and moment intensity levels.

3.3 Best, Average, and Worst Dipole Orientation

For one dipole, the lower bound error analysis for EEG generates a seven by seven dimensional covariance matrix: one dimension for the noise variance, three dimensions for the moment, and three dimensions for the location. In the case of MEG, we only have two dimensions of the moment we can estimate, but in either case we always have three dimensions assigned to the location. If we use Cartesian coordinates for our location parameters, then the difference vector between our estimate of the location and the true location can be written as

$$\text{Location Error Vector} = \left[(x-\hat{x}), (y-\hat{y}), (z-\hat{z}) \right]. \qquad \text{(EQ 16)}$$

The corresponding (3 x 3) submatrix bounding the error covariance for these parameters would be represented as

$$\mathrm{CRLB}(\vec{l}) = \begin{bmatrix} \sigma_{xx}^2 & \sigma_{xy}^2 & \sigma_{xz}^2 \\ \sigma_{xy}^2 & \sigma_{yy}^2 & \sigma_{yz}^2 \\ \sigma_{xz}^2 & \sigma_{yz}^2 & \sigma_{zz}^2 \end{bmatrix}. \qquad \text{(EQ 17)}$$

This bounding matrix can be represented by an error ellipsoid, independent of our choice of coordinate systems. The major axes of the ellipsoid are found as the eigenvectors of the bounding matrix. The lengths of the axes are found from the corresponding eigenvalues. The eccentricity of the ellipsoid gives an indication of the directional bias that the error vectors will exhibit. Indeed, the minor axes of the ellipsoid represent the "preferred directions" discussed in (Cohen and Cuffin, 1983). If we consider the errors in any direction to be equally important, then we can ignore this directional bias and instead focus on the scalar length of this error vector. The lower bound on the expected squared value of this length is the sum of the eigenvalues, or equivalently, the trace (sum of the diagonal elements) of the bounding matrix. Hence, at a given location $\vec{l}$ and for a given moment $\vec{q}$, we can define our scalar localization error bound in Cartesian coordinates as

$$\text{RMS Location Error: } \sigma_{\vec{l}}(\vec{l}, \vec{q}) = (\sigma_{xx}^2 + \sigma_{yy}^2 + \sigma_{zz}^2)^{\frac{1}{2}} \qquad \text{(EQ 18)}$$

which has the physical interpretation of being the lower bound on the root mean square (RMS) length of the three-dimensional error vector given by (16).

We emphasize in (18) the dependency of this calculation on the moment of the dipole; different moment directions at the same location will generate, in general, different error ellipsoids. Since radial sources represent "silent sources" for MEG data, we will largely restrict our examination to sources lying in the tangential plane for both MEG and EEG data. This restriction also simplifies our analysis of the RMS location error, since now the moment orientation can be parameterized by a single parameter θ describing the angle the moment makes in the tangential plane.

For a given point $\vec{l}$, we can "scan" over all possible θ, observing the RMS location error. Fig. 3 presents just such a scan for two different cases. We see a strong dependency on the dipole orientation for one situation and relatively little dependency for the other. We

retain three values from these curves: the best (lowest) RMS error, the worst, and the average over all angles. We will illustrate in the examples below the sensitivity of some sensor patterns to dipole orientation.

For two dipoles, we extend the above approach. Since two dipoles represent six location parameters, we have a six dimensional bounding matrix which represents all of the correlations between the parameters. If we focus on the error vectors extending from the true locations to the estimated locations, we can still interpret the sum of the first three diagonal terms as the lower bound on the mean square error for the localization of the first dipole. The complexity is that *each* RMS error length is dependent on *both* dipole moments and *both* locations. We can express these RMS values using the six diagonal terms of the bounding matrix, expressed here in Cartesian coordinates as

$$\sigma_{\vec{l}_1}(\vec{l}_1, \vec{q}_1, \vec{l}_2, \vec{q}_2) = (\sigma^2_{x1x1} + \sigma^2_{y1y1} + \sigma^2_{z1z1})^{\frac{1}{2}}$$

$$\sigma_{\vec{l}_2}(\vec{l}_1, \vec{q}_1, \vec{l}_2, \vec{q}_2) = (\sigma^2_{x2x2} + \sigma^2_{y2y2} + \sigma^2_{z2z2})^{\frac{1}{2}} \qquad \text{(EQ 19)}$$

If we again restrict the moments of both dipoles to lie in the tangential plane, we can parameterize these scalars as functions of angles for each moment. For a given pair of dipole locations, $(\vec{l}_1, \vec{l}_2)$, we scan over all possible combinations of θ_1 and θ_2 and again find the best, worst, and average RMS lengths for each dipole. In general, the best orientation occurs when the two moments are arranged orthogonally, such that the peak intensities of the dipoles are well separated in the field array. The worst arrangement is for both dipoles to be aligned in the same direction, such that their intensity peaks coincide and lie poorly across the array.

4.0 Monte Carlo Simulation

All of the results presented in this paper represent the lower bound on the variance of the estimated location parameters for any unbiased estimator. In this section, we present the results of a Monte Carlo simulation based on a standard least squares estimator for a 37 sensor MEG instrument. The full CRLB analysis assumptions are presented in Section 5.0 and the specific details of the 37 sensor arrangement are presented in Section 5.9, but we present first these Monte Carlo results both as a confirmation of the formulas and to

demonstrate the closeness of the CRLBs to the actual RMS error results of our Monte Carlo study.

For each point on a four mm grid across the positive quadrant of the x-z plane, we positioned a dipole in the best moment orientation as found by our CRLB analysis. We synthesized the single dipole forward model across the array using the same dipole intensity as in the analysis, then added 100 realizations of zero mean white Gaussian noise at the sensors, using a random number generator with the same standard deviation as used in the analysis. We then estimated the dipole location parameters for each noise realization using the Nelder-Meade nonlinear least-squares approach described in (Mosher et al., 1992). We initiated the search within a 10 mm region around the true location, so as to enhance the possibility of finding the global minimum and avoid converging instead into a local minimum.

From the locations estimated for each of the 100 data sets at each dipole location, we computed the RMS location error for that position. Fig. 4 presents the results, along with the corresponding CRLB analytic results. In all regions where the anticipated standard deviation was less than a few centimeters, we see excellent agreement between the analysis and the simulations. In the deeper regions, the signal received at the array plummets into the noise due to the distance to the dipole. The standard deviation in these regions is quite high, and the minimization algorithm often fails to reasonably converge. Even given this poor array SNR, the simulation results agree well with the lower bound results. The overall result is a confirmation of both the MEG CRLB formulas and the evidence that the least-squares estimator comes very close to meeting the CRLB.

At a four mm spacing, the MEG Monte Carlo simulation here required several days of computation on a Sun SPARCstation 2 computer, since each error trial may itself require many hundreds of calls to the generating function, and at each point in the grid we are performing 100 trials. The equivalent EEG model would require an order of magnitude greater processing time, due to the complexity of its gain transfer function. This computational burden for just a single Monte Carlo study with only a single dipole orientation underscores the utility of the CRLB calculations in more rapidly assessing many sensor arrangements and all dipole orientations.

5.0 EEG and MEG Analysis Examples

The formulas presented above for the dipole in a four concentric sphere model are general for arbitrary sphere radii, tissue and skull conductivities, sensor and dipole locations, dipole intensities and orientations. The CRLB formulas presented in the Appendix are also for the general spatio-temporal model. Here we restrict our numerical analysis to a few relatively simple cases of symmetric array patterns and one or two dipoles. The CRLB formulas require the calculation of the partial derivatives of the gain matrix with respect to the unknown location parameters. The tedious calculations for the EEG model were carried out by hand and then verified using MapleV, a symbolic algebra computer program. The MEG partials were straightforward.

5.1 Analysis Region

Fig. 2 displays one of the array patterns used here with relation to the spherical model. The other patterns were similarly symmetric about the z-axis, which runs through the center of the array. Due to this high degree of symmetry, we restrict our analysis region to just the positive x-z plane. The error results in this one plane can then be inferred by symmetry for the entire upper hemisphere. In reality, as this analysis plane is rotated about the z-axis, differences will arise due to the finite spacing of the sensors; however, the differences are not anticipated to be great.

5.2 Dipole Orientation

One of the goals of this study was to allow careful and cautious comparisons between EEG and MEG data. For the simple dipole in a sphere model used here, the radially oriented dipole generates no external magnetic field, so EEG holds an obvious advantage. We thus restricted the orientation of the dipole to lie in the tangential plane for both the EEG and MEG data for most of the error analyses presented below. This restriction also simplified the parameterization of the dipole orientation to the single parameter θ, the angle the moment makes in the tangential plane. We note that this is not unduly restrictive, since all of the results presented here scale with dipole intensity Q. In the case of MEG data, a dipole with a radial component and an intensity Q would simply project into the tangential plane as a dipole with intensity $Q\cos\phi$, where ϕ is the angle the dipole makes with respect to the tangential plane. All of the standard deviations for the MEG data presented here could

then be appropriately scaled for inclusion of any desired radial component. We present also for comparison some EEG results with no restriction on the dipole moment orientation and find that the results are not much different than for the tangential dipole study.

5.3 Dipole Intensity

The bounds presented in (15) could be normalized to the ratio v/Q^2, but these units of sensor noise variance v to dipole intensity Q are non-intuitive and do not give the user any relative feel for the absolute localization error. We therefore attempt to establish some realistic values for the dipole intensity, and in the next section, the noise variance. We note that this ratio can be viewed as a signal-to-noise ratio, defined here as SNR(dipole) = Q/σ, where σ is the standard deviation. By fixing the dipole intensity at Q, then moving this dipole about the upper hemisphere, the actual signal intensity received by the sensor array will vary roughly as the inverse function of the squared distance to the array. Hence, if we consider a second definition, SNR(array), to be a function of the signal at the array (either an average across all sensors or the peak field among all sensors), then we observe that SNR(array) will drop as the dipole is moved deeper. To maintain SNR(array) as a constant over all dipole locations requires that deeper dipoles have correspondingly stronger intensities.

Variations of SNR(array) are common definitions in other studies, including (Cuffin and Cohen, 1979; Cuffin, 1986; Mosher et al., 1990; Oshiro et al., 1992), with one benefit being that one does not need to assign explicit units of amps to the dipole current. In these other studies, all calculations are carried out in "relative units", where the dipole intensity is set to one unit, and the noise standard deviation is set to some ratio of this unit, for instance, ten percent. We argue that SNR(dipole) is the preferred definition where the intent is to study the location error for a dipole or sets of dipoles arbitrarily located in the head. Adjusting the dipole intensity as a function of location leads to distorted comparisons between different array configurations, since dipole intensity has implicitly become a function of sensor location, and, in this study, as a function of sensor type, EEG or MEG. Deeper dipoles may also be assigned unrealistically high currents simply to keep the SNR(array) constant. A fixed dipole intensity at a physically plausible current leads to a possibly more informative accuracy analysis and more direct comparisons between configurations.

In (Cohen and Cuffin, 1983), a relatively strong dipole was estimated to have a dipole intensity of 2.1 μA-cm (21 nA-m). In (Cohen et al., 1990), an implanted dipole of 16 mm length was stimulated with 4 μA current, for an equivalent 64 nA-m current dipole. Since we wished to establish a baseline dipole intensity that was readily scaled to other intensities, that was of the proper order of magnitude, and that appeared physically plausible, we selected 10 nA-m as our dipole intensity. This selection allows us to present accuracy bounds in units of meters, but we emphasize that all bounds displayed can easily be rescaled with some other choice of dipole intensities.

5.4 Noise Intensity

The selection of a standard deviation for the noise is not immediately obvious, in part due to the wide-spread practice of averaging experimental data. In theory, we could average the trials until the noise is reduced to any arbitrary low value. The noise standard deviation also presents the problem in this EEG/MEG comparison of being in units of either volts or teslas, respectively; unlike the dipole intensity Q, we cannot easily set a standard deviation general to both sensor types.

A dipole of intensity 10 nA-m near the cerebral spinal fluid layer can generate a field peaking on the order of 300 fT or 4 μV in nearby sensors, for the sensor patterns and model examined in this paper. In research such as (Cuffin, 1986), the standard deviation is expressed as a percentage of the peak, approximately ten percent. This definition roughly translates into similar SNRs examined in (Westerkamp and Aunon, 1987; Stok, 1987; Achim et al., 1991). We therefore somewhat arbitrarily set the MEG noise standard deviation to 35 fT and the EEG noise standard deviation to 0.4 μV, to reflect this 10:1 ratio. We compare with (Balish et al., 1991), who had a stated noise level of 50 fT after averaging 200 trials. We note the difficulty in extracting absolute noise levels from other reports for comparison, due to the wide-spread practice of normalizing the noise standard deviation into the field levels.

5.5 Sensor Assumptions

In all cases, the EEG sensors are assumed to be affixed directly to the 88 mm scalp sphere and acquire an absolute voltage potential referenced to "infinity." In reality, EEG measurements are acquired as differential measurements with reference to a common local

sensor or adjacent sensors. We ignore here this common use of a "switching" matrix. We also ignore the physical diameters of the sensors and assume they make a point voltage measurement.

The MEG coils are placed 105 mm from the head center, representing a 17 mm offset from the scalp surface. This distance was chosen to represent the dewar wall thickness of the larger sensor arrays and the air gap, both of which prevent the placement of the coils closer to the subject's scalp. Although these coils are often 20 mm in diameter, we also assume that they make a point magnetic field measurement and are oriented in the radial direction. (Jeffs et al., 1987) showed that this practice is a reasonable approximation by comparing point models with integrations across the coil diameters. Since most MEG sensors are arranged in a first or second order gradiometer configuration to control external field noise, we ran a CRLB comparison between a perfect point measurement and a perfect first order gradiometer, with a coil baseline separation of 50 mm. Our CRLB results for a 37 channel comparison showed only minor differences in the deep regions of the upper hemisphere. Thus, to keep the comparisons simpler, we ignored any considerations of gradiometers for the MEG examples presented here.

5.6 Array Patterns

The sensor array patterns presented here are identically arranged in angular separation for both EEG and MEG cases and were designed to mimic possible MEG sensor patterns, since MEG sensors are much larger than EEG probes. Although EEG probes are much smaller, they too have practical limitations in surface adjacent placement due to considerations of gels forming salt bridges for electrodes too closely spaced. In the following examples, we present the error lower bounds for 127 sensors spread both over the entire upper hemisphere and then densely in one region. We then present for comparison the results for just thirty-seven sensors in an array pattern similar to that of the commercially available thirty-seven sensor MEG instruments; the 127 sensor dense pattern was chosen to cover the same spatial area as the thirty-seven channel system. We also present for comparison the potential accuracy possible using the standard EEG Ten-Twenty array pattern, which provides a wide spatial coverage similar to the 127 pattern presented, but at a much more sparse spatial sampling.

The overall emphasis is to show accuracies possible for either wide spatial coverage or dense local coverage, or the accuracy available with an array pattern similar to that of the

presently existing technologies or practices. Direct comparisons among different EEG and different MEG patterns are warranted, since dipole intensity and noise were held constant; however, comparisons between EEG and MEG results must consider the differences in noise assumptions and the uncertainties in model parameters. While the MEG model presented here is relatively simple, the equivalent simple EEG model is dependent on many more assumptions of conductivities and sphere radii.

5.7 Upper Hemisphere 127 Sensor Pattern Results

We designed a simple pattern to cover the entire upper hemisphere without placing sensors too close together. The first sensor is placed on the z-axis, then six sensors are placed evenly around a circle located fifteen degrees down from the z-axis. The next ring is located thirty degrees from the z-axis, along which are evenly arranged twelve sensors. The pattern is repeated at fifteen degree intervals for a total of six rings, with the rings containing six, twelve, eighteen, twenty-four, thirty, and thirty-six sensors, respectively, for a total of 127 sensors. The last ring lies completely in the x-y plane, giving us full upper hemisphere spatial coverage. The MEG sensors were oriented radially.

This pattern was chosen as a natural extension of commercially available seven and thirty-seven channel MEG sensor arrays. The sensors are spaced roughly two centimeters apart, which is about the diameter of a single MEG coil. In design phases now are EEG and MEG instruments with roughly 100 sensors. The analysis here for 127 sensors should represent reasonably well the potential accuracy of these new instruments, if used for whole head coverage.

5.7.1 One Tangential Dipole

The first study calculated the lower bound for a single dipole located anywhere in the positive x-z plane ($y = 0$). The dipole was stepped along at one millimeter intervals within the brain sphere. At each location, the moment angle was stepped in one degree increments from 0 to 179 degrees, and at each angle the RMS lower bound was calculated using (18). The average RMS lower bound was calculated over all 180 degrees and the best and worst angles located. At these extrema, a minimization or maximization algorithm was initiated to refine the estimate of the best and worst RMS errors, respectively. Three different bounds were retained for each location point in the grid representing the best, average, and worst RMS errors.

Fig. 5 and Fig. 6 respectively show these results for the EEG and MEG cases as contours representing lines of equal RMS error. We note that along the z-axis, the dipole is in the center of a symmetric array, and the three plots show no difference in accuracy as a function of moment orientation. Along the x-axis, this array symmetry does not hold, and here we see the strong dependency on both location and moment orientation due to the edge effects of the array. For much of the upper head region, the error curves are approximately concentric, so that for this upper hemisphere sensor pattern RMS lower bounds are primarily a function of radial depth and free of orientation consideration.

Since dipole sources oriented radially produce no external magnetic field, we see increasing MEG error for dipoles located progressively near the center. In contrast, the EEG error near the center flattens out, a consequence of this inner region being approximately equally located from all sensors. Near the surface of the sphere, both modalities exhibit similar changes in error as a function of radial depth.

5.7.2 Two Tangential Dipoles

We now examine the rapid degradation in performance that occurs by introducing a second dipole. For simplicity in examining the effect of an additional dipole on the localization accuracy of the original dipole, we fixed the location of the second dipole on the z-axis at z=7.5 cm, directly under the center of the array. Both dipoles had equal intensity Q, such that all results are still directly scalable to any other arbitrary intensity. By the symmetry of the location of the additional dipole on the z-axis, we can still restrict our analysis region to the positive x-z plane and infer the results for the remainder of the upper hemisphere.

As in the single dipole studies, the first dipole was stepped along on a one mm grid within the positive x-z plane. At each location point, the angles of *both* of the dipoles were stepped in ten degree increments from 0 to 170 degrees, resulting in a grid of 18 by 18 different angle combinations. For each angle pair, the RMS error bounds for the first dipole were calculated as defined by (19). The average errors were then calculated from this two-dimensional grid of error bounds and the best and worst angle pairs found. At these grid point extrema, a Nelder-Meade simplex minimization or maximization algorithm was initiated to refine the estimate of the best or worst RMS error bounds.

Fig. 7 and Fig. 8 present the results for the EEG and MEG cases, respectively. Unlike the single dipole, here we note the strong dependency on dipole orientation. A wide

range of error is possible between best and worst orientation pairs. Comparing with the one dipole case above, we note that along the x-axis the results do not differ much, since the additional dipole on the z-axis is far enough away as to have little effect. As we follow along the inner radial CSF layer, we see that the second dipole can affect the accuracy of the first dipole as far as four cm away, rapidly doubling the standard deviation error. In general, the best moment orientation pairs were such that the two dipoles pointed in orthogonal directions, so that their corresponding field intensities across the array were best separated. The worst orientation pairs pointed both dipoles in the same parallel direction, so that their surface potentials had the greatest overlap and the peaks of intensities fell poorly across the array.

This study has presented only a few of the endless possible combinations for two dipole intensities and positions. However, this one study does show the rapid degradation in accuracy that occurs when trying to localize two equal intensity dipoles that are relatively well situated within the array. We also see that localization error is not simply a function of the relative distance between the two dipoles, but much more complexly related as a function of absolute dipole position and orientation. We contrast this with the results in (Oshiro et al., 1992). Through a limited Monte Carlo analysis (Oshiro et al., 1992) erroneously claim to show that the error is a function of only the distance between dipoles and does not depend on the orientation. While this may be true in specific instances, it is clearly not true in general. By comparing the best and worst standard deviation curves presented here, we see that their conclusion applies only to limited regions of the sphere. In general, the relative orientation between the two dipoles is very important.

5.8 Dense 127 Sensor Pattern Results

The upper hemisphere pattern examined above exhibited some variations near the inner surface of the CSF, primarily due to the somewhat coarse two centimeter spacing of the sensors. Here we examine the same 127 probes concentrated in a much smaller region, to observe more directly the effects of spatial sampling. The array was constructed as above with six rings of sensors, but now the spacing between each circle and the z-axis was in six degree increments, rather than fifteen degrees. The MEG sensors were oriented radially. The result was an array that subtends a 72 degree angle, which is approximately the same spatial coverage as that of the commercially available 37 channel MEG instruments, but with much denser spatial sampling. Here, the spacing is in general less than one centimeter between

sensors, which would prove to be impossible for the larger MEG coils and daunting for the placement of surface EEG electrodes. Hence this case might represent one of the densest patterns presently possible for either modality.

5.8.1 One Tangential Dipole

The analysis procedure here was identical to that of the 127 sensor upper hemisphere pattern. Fig. 9 and Fig. 10 respectively display the results for the EEG and MEG cases. Here we note the immediate impact the limited spatial coverage has on overall dipole accuracy and particularly the increased sensitivity to moment orientation due to the array edges. Directly under the array, where array edge effects are minimized, we see an overall factor of root two improvement in the RMS error bounds relative to the upper hemisphere array, due to the increased number of sensors in the proximity of the dipole. The error bound rises rapidly in the lower regions of the sphere due to the combined effects of squared distance to the sensor array and poor spatial coverage of the field peaks. This latter effect is most notable on the deeper dipoles located directly on the z-axis. For a fixed value of z, we can come out on the x-axis and see an improvement in error, most notably for the best moment analysis. By offsetting the deeper dipoles from the center of the array, we are able to position the peak of the field intensity such that it falls across the array.

Comparing EEG and MEG results, we see that MEG suffers more rapidly in the lower regions as a function of the three effects of depth, proximity to the sphere center, and poor spatial coverage. By comparison, EEG has a more gradually increasing error as a function of just the two effects of depth and coverage.

5.8.2 Two Tangential Dipoles

The analysis procedure here was identical to that of the two dipole study for the 127 upper hemisphere pattern. Fig. 11 and Fig. 12 present the results of the two dipole study for the EEG and MEG cases. The lower bounds in the deep regions and regions outside of the array have risen sharply, compared to their one dipole counterparts. Compared to the two dipole 127 upper hemisphere pattern in Fig. 7 and Fig. 8, the increased sensor density here does allow the two dipoles to be placed somewhat closer together, but the edge of the array confines the region with low error bounds to a relatively small area.

5.9 Thirty-seven Sensor Pattern Results

In this study, we arranged three rings of sensors, each spaced in increments of 12 degrees from the z-axis and containing six, twelve, and eighteen sensors respectively, for a total of 37 sensors, as displayed in Fig. 2. The MEG sensors were oriented radially. This pattern approximates that of commercially available thirty-seven channel MEG instruments. We note that the 127 sensor upper hemisphere pattern examined above is slightly coarser in spatial sampling than this thirty-seven channel pattern (15 degree spacing versus 12 degree), but covers a wider spatial area. The 127 sensor dense pattern described above has the same spatial coverage as the 37 channel instrument at roughly twice the spatial sampling density.

5.9.1 Single Tangential Dipole

The analysis procedure was identical to that of the127 sensor upper hemisphere study. Fig. 13 and Fig. 14 respectively show the EEG and MEG case for the single dipole restricted to the tangential plane. The accuracy directly under the array is comparable to that of the upper hemisphere array, but the accuracy declines much more rapidly as a function of depth. Also noticeable is the strong dependency on dipole orientation, similar to that of the dense array above. The overall effect is a greatly reduced area directly under the array that has an accuracy comparable to that of the larger arrays. The comparison between EEG and MEG errors follows that of the dense array analysis above.

5.9.2 Two Tangential Dipoles

The two dipole analysis procedure was identical to that of the 127 sensor upper hemisphere study. Fig. 15 and Fig. 16 respectively show the EEG and MEG RMS error bounds of a dipole when an additional dipole of equal intensity was placed on the z-axis at z=7.5 cm. Here we see almost no region where the dipole's error bound hasn't at least doubled from the single dipole study. In the worst case, we also found that it is impossible to place two dipoles on the z-axis in the same orientation and still resolve them. This perfect array ambiguity is a consequence of the three perfectly symmetric rings of sensors. The best orientation pairs were again in general orthogonal to each other, and we see that in general the overall accuracy region has been greatly reduced.

5.9.3 EEG Single Unconstrained Dipole

The above studies restricted the dipole to the tangential plane, so that comparisons might be more readily made with the between EEG and MEG results. In this study, we allow the EEG dipole to be unconstrained in orientation, to observe if there was any significant improvement. We used the 37 sensor arrangement above, and at each location point we calculated all possible combinations of radial and tangential moment orientations in ten degree increments over the range 0 to 170 degrees. The minimization/maximization analysis was carried out in a manner identical to the two dipole studies above, except in this study the two angles were for the one dipole.

Fig. 17 displays the best, worst, and average EEG RMS error bounds for the single unconstrained dipole. In the near region of the array there was only a slight improvement of the best and a slight degradation of the worst, but that on average the results did not change remarkably, as compared to the results presented in Fig. 13. In the deeper regions, the relaxation of the tangential restriction allowed the dipole to swing into a radial direction and direct more of its surface potential across the array, thereby smoothing the error curves in these deeper regions; the error values are nonetheless still quite comparable to the tangentially restricted dipoles. Overall, the tangential restriction used above allowed for simpler studies, since the moment was only a function of one angle parameter, and the tangential restriction does not appear to have seriously degraded the localization accuracy.

5.10 EEG Ten-Twenty Sensor Pattern Results

Since EEG data have historically been collected in the Ten-Twenty array pattern using 21 electrodes, we performed a study of this twenty-one sensor pattern, which has the feature of wide spatial coverage and poor spatial sampling. Fig. 18 shows the results for the best orientation, again using the same analysis procedure as for the other studies. We note that a source directly underneath the sensor at approximately x=6 cm and z=6 cm does not improve significantly in accuracy over radially deeper sources. Although a shallow source generates a significantly stronger signal at the surface, the spatial undersampling is such that only one nearby sensor receives a significant signal. One sensor cannot adequately locate the source, regardless of the source intensity. The deeper sources generate a signal across enough surface sensors to compensate for their relatively weaker surface signal. The overall

effect of this sparse array of sensors is a relatively flat and larger error surface compared to the other studies.

5.11 EEG and MEG Fusion

The field pattern generated by a dipole across an array of EEG sensors roughly peaks along the axis of the dipole moment. In contrast, the MEG pattern peaks to the sides of the dipole moment, roughly perpendicular to the EEG pattern. In this study, we assume both EEG and MEG data are acquired and observe the improvement generated by this diversity in the information content. The sensor pattern was the same as the thirty-seven system described above, except that here we have a total of 74 measurements for the two combined sensor systems. The analysis procedure was identical to the other studies. Unlike the other studies, the results presented here do *not* scale with arbitrary dipole intensity and noise variance, since we must consider both the EEG and MEG noise simultaneously. To bring the two modalities into relatively scaled units, one of the arrays must be multiplied by the ratio of the two noise variances, introducing a more complex relationship between standard deviation, dipole intensity, and noise variances.

Fig. 19 shows fusion of a dipole restricted to the tangential plane. In contrast with Fig. 13 and Fig. 14 for the same array pattern and respective noise variances, we note almost no difference among the best, worst and average moment orientations here. Since the EEG and MEG arrays complement each other so well in their field patterns, the dipole always points in a direction that is captured well by one of the two arrays. In the regions directly below the center of the array, we note an improvement simply due to having twice as many measurement points. In the deeper regions, the EEG sensors have obviously improved the response near the center, but we see that both sensor modalities have greatly improved the other deep regions.

This analysis confirms the statements of (Cohen and Cuffin, 1983; Anogianakis et al., 1992; Therapeutics and Technology Assessment Subcommittee, 1992) concerning the potential in directly combining EEG and MEG measurements into an overall superior resolution ability, unachievable by either modality alone. One extension of this study would be to augment fixed MEG sensor arrays with a smaller array of EEG sensors to determine if similar improvements can be obtained.

6.0 Discussion

The results presented in these studies focused on the single time slice problem, but the formulas presented for the CRLB are for the more general temporal problem. The CRLB formulas show the nonlinear improvement achievable by considering multiple time slices; in the simplest case of fixed dipole moment, the standard deviations are at minimum improved by the square root of the number of time slices. If the time series of the dipole moments have any algebraic independence, the results are even further improved. An addition to the formulas would be the inclusion of the fixed moment dipole model, which would improve the lower bounds by incorporating the knowledge that the dipole does not "rotate"; however, the "rotating" formulas presented here are more general. The work of (Baumgartner et al., 1991; Achim et al., 1991) may have benefited from the use of these spatio-temporal CRLBs as a rapid analysis tool in interpreting their specific case studies of dipole locations and time series.

The RMS errors presented in this study do not consider the directional bias that might occur. In the case of EEG and MEG, with data measured from external sensors (i.e, no invasive probes), the direction of greatest localization error will in general be in the radial direction, since the tangential directions are more accurately measured by the surface arrays (the "preferred directions", as noted by (Cohen and Cuffin, 1983)). If we were to model the cortex as a simple thin shell beneath the skull, then we might be able to ignore this radial error; the tangential errors were in general much smaller. In reality, the cortical folds (analyzed in some detail in (Kaufman et al., 1991)) force consideration of the radial location of the dipole as well. In the absence of any prior information as to the importance of one direction over another, we argue here that error in any direction is important.

The approaches presented here will also assist analysis of novel sensor locations, orientations, and parameter sensitivities by providing a preliminary CRLB baseline. We emphasize that while small CRLB bounds will not guarantee that such standard deviations will ever be achievable, large CRLB bounds will steer us clear of situations where the desired accuracy would be impossible.

7.0 Acknowledgments

We thank Chris C. Wood and the Biophysics Group at the Los Alamos National Laboratory for their early reviews and comments on the preliminary results of this study.

Appendix Cramer-Rao Derivation

In this appendix, we derive the Fisher Information Matrix and the corresponding Cramer-Rao lower bound for the general spatio-temporal model.

We define some notation and develop the bound to parallel the work of (Stoica and Nehorai, 1989). We define **D** as the partials of the gain matrix **G**:

$$\dot{l}_k \equiv [l_{xk}, l_{yk}, l_{zk}]$$

$$\mathbf{d}(l_{xk}) \equiv \frac{\partial}{\partial l_{xk}} \mathbf{G}(\dot{l}_k)$$

$$\mathbf{d}(\dot{l}_k) \equiv [\mathbf{d}(l_{xk}), \mathbf{d}(l_{yk}), \mathbf{d}(l_{zk})]$$

$$\mathbf{D} \equiv [\mathbf{d}(\dot{l}_1), \ldots, \mathbf{d}(\dot{l}_k), \ldots, \mathbf{d}(\dot{l}_p)] \qquad \text{(EQ 20)}$$

where l_{xk} refers to the x-axis component of the k^{th} dipole location, and similarly for the other subscripts. Arrange the p moments at the j^{th} time slice, $\underline{q}(j)$, into a block diagonal matrix,

$$\mathbf{X}(j) \equiv \begin{bmatrix} \mathbf{I}_3 \otimes \hat{q}_1(j) & & \mathbf{0} \\ & \cdots & \\ \mathbf{0} & & \mathbf{I}_3 \otimes \hat{q}_p(j) \end{bmatrix} \qquad \text{(EQ 21)}$$

where $\mathbf{I}_3$ is a 3 x 3 identity matrix and " $\otimes$ " denotes the Kronecker product.

With our parameters and their partials thus redefined into the matrices **G**, **D**, and **X**, we group these together into two more matrices before deriving the Fisher Information

Matrix. This notation also simplifies the expressions for inverting the FIM to obtain the lower bounds:

$$\Gamma \equiv \sum_{j=1}^{n} [\,(\mathbf{DX}(j))^{T}(\mathbf{DX}(j))\,]$$

$$\Delta(j) \equiv \mathbf{G}^{T}\mathbf{DX}(j)$$

$$\Delta \equiv [\Delta(1)^{T}, \ldots, \Delta(n)^{T}]^{T} \qquad \text{(EQ 22)}$$

Thus for m sensors, n time slices, additive zero-mean white noise with a variance ν, and the dipole moments and locations grouped as defined above, the Fisher Information Matrix is (Stoica and Nehorai, 1989)

$$\mathbf{J} = \frac{1}{\nu}\begin{bmatrix} \frac{mn}{2\nu} & 0 & 0 \\ 0 & I_n \otimes \mathbf{G}^{T}\mathbf{G} & \underline{\Delta} \\ 0 & \underline{\Delta}^{T} & \Gamma \end{bmatrix}. \qquad \text{(EQ 23)}$$

The three diagonal elements represent the information content of the scalar noise variance, the set moment parameters, and the set of location parameters, respectively. The off-diagonal terms represent the cross-information between the various parameters. With this partitioning and use of the standard matrix inversion formulas (Sorenson, 1985), we can readily invert this matrix analytically. We are particularly interested in the diagonal elements, since the Cramer-Rao lower bound for the ith parameter ψ_i is simply the ith diagonal element of J^{-1} (Sorenson, 1985).

The off-diagonal zero elements in **J** make the lower bound for the scalar noise variance particularly easy to calculate,

$$\mathrm{CRLB}(\nu) = \frac{2\nu^{2}}{mn} \qquad \text{(EQ 24)}$$

The lower bound covariance matrix for all p locations in $\underline{l}$ is found in the lower 3p x 3p portion of matrix $\mathbf{J}^{-1}$,

$$\mathrm{CRLB}(\underline{l}) = \nu\,[\Gamma - \Delta^{T}[\mathbf{I}_n \otimes (\mathbf{G}^{T}\mathbf{G})^{-1}]\,\Delta]^{-1} \qquad \text{(EQ 25)}$$

$$= \nu\left[\sum_{j=1}^{n} (\mathbf{DX}(j))^{T}\,\mathbf{P}_{G}^{\perp}\,(\mathbf{DX}(j))\right]^{-1}. \qquad \text{(EQ 26)}$$

where $\mathbf{P}_{G}^{\perp} = (\mathbf{I} - \mathbf{G}\mathbf{G}^{\dagger}) = (\mathrm{I} - \mathbf{P}_{G})$ is the orthogonal complement of the projection matrix for $\mathbf{G}$, and $\mathbf{G}^{\dagger}$ is the pseudoinverse of $\mathbf{G}$, $\mathbf{G}^{\dagger} = (\mathbf{G}^{T}\mathbf{G})^{-1}\mathbf{G}^{T}$.

The lower bounds for the moment series at each time slice j can be readily expressed in terms of the lower bound for the location. If we define $\gamma \equiv \mathrm{CRLB}(\underline{L})/\nu$, then the lower bound covariance matrix for *each* moment time slice j, j = 1,...,n is

$$\mathrm{CRLB}(\underline{q}(j)) = \nu\,[\,(\mathbf{G}^{T}\mathbf{G})^{-1} + \mathbf{G}^{\dagger}\mathbf{DX}(j)\gamma(\mathbf{G}^{\dagger}\mathbf{DX}(j))^{T}\,]\,. \qquad \text{(EQ 27)}$$

References

Achim A, Richer F, Saint-Hilaire JM, "Methodological considerations for the evaluation of spatio-temporal source models," *Electroenceph. clin. Neurophysiology.*, 1991, 79: 227 - 240.

Ahlfors SP, Ilmoniemi RJ, Hamalainen MS, "Estimates of visually evoked cortical currents" *Electroenceph. clin. Neurophysiology.*, 1992, 82: 225 - 236.

Anogianakis G, Badier JM, Barret G, et al. "A consensus statement on relative merits of EEG and MEG," Editorial, *Electroenceph. clin. Neurophysiology.*, 1992, 82: 317 - 319.

Arthur RM, Geselowitz DB, "Effect of inhomogeneities on the apparent location and magnitude of a cardiac dipole source," *IEEE Trans. Biomedical Eng*, 1970, 17: 141-146.

Ary JP, Klein SA, and Fender DH, "Location of sources of evoked scalp potentials: corrections for skull and scalp thicknesses," *IEEE Trans. Biomedical Eng.*, 1981, 28: 447-452.

Balish M, Sato S, Connaughton P, and Kufta C. "Localization of implanted dipoles by magnetoencephalography," *Neurology* 1991; 41:1072-1076.

Baumgartner C, Sutherling WW, Di S, and Barth DS, "Spatiotemporal modeling of cerebral evoked magnetic fields to median nerve stimulation," *Electroenceph. clin. Neurophysiol.*, 1991, 79: 27 - 35.

Brody DA, Terry FH, and Ideker RE, "Eccentric dipole in a spherical medium: generalized expression for surface potentials," *IEEE Trans. Biomedical Eng.*, 1973, 20:141-143.

Cohen D, and Cuffin BN, "Demonstrations of useful differences between magnetoencephalogram and electroencephalogram," *Electroenceph. clin. Neurophysiol.* 1983, 56:38-51.

Cohen D, Cuffin BN, Yunokuchi K, Maniewski R, Purcell C. Cosgrove GR, Ives J, Kennedy JG, Schomer DL. "MEG versus EEG localization test using implanted sources in the human brain," *Ann Neurol* 1990, 28:811-817.

Cuffin BN, Cohen D, "Comparison of the magnetoencephalogram and electroencephalogram," *Electroenceph. clin. Neurophysiol.*,1979, 132-146.

Cuffin BN, "Effects of measurement errors and noise on MEG moving dipole inverse solutions," *IEEE Trans. Biomedical Eng.*, 1986, 33: 854 - 861.

Cuffin BN, "Effects of head shape on EEG's and MEG's," *IEEE Trans. Biomedical Eng.*, 1990, 37:44-52.

Cuffin BN, "Eccentric spheres models of the head," *IEEE Trans. Biomed. Engr.*, 1991, 38: 871-878.

Cuffin BN "Moving dipole inverse solutions using MEGs measured on a plane over the head," *Electroenceph. clin. Neurophysiol.*, 1991, 78: 341 - 347.

De Munck JC, "The estimation of time varying dipoles on the basis of evoked potentials," *Electroenceph. clin. Neurophysiol.*, 1990, 77: 156-160.

De Munck JC, Van Dijk BW, and Spekreijse, H, "Mathematical dipoles are adequate to describe realistic generators of human brain activity," *IEEE Trans. Biomedical Eng.*, 1988, 35:960-966.

Hari, R., Hamalainen M, Ilmoniemi, R. Lounasmaa, OV. "MEG versus EEG localization test," Letter to the Editor, *Ann Neruol.* 1991, 30: 222-223.

Ilmoniemi RJ, Hamalainen MS, and Knuutila J, " The forward and inverse problems in the spherical model," *Biomagnetism: Applications and Theory*, ed. Wienberg, H., Stroink, G. and Katila, T. 1985, Oxford: Pergamon 278-282.

Jeffs B, Leahy R, Singh M, "An evaluation of methods for neuromagnetic image reconstruction," *IEEE Trans. Biomedical Eng.*, 1987, 34:713-723.

Kaufman L, Kaufman JH, Wang, JZ. "On cortical folds and neuromagnetic fields," *Electroenceph. clin. Neurophysiol.*, 1991, 79: 211 - 226.

Kavanaugh RN, Darcey TM, Lehmann D, and Fender DH, "Evaluation of methods for three-dimensional localization of electrical sources in the human brain," *IEEE Trans. Biomedical Eng.*, 1978, 25:421-429.

Korn GA, and Korn TM, *Mathematical Handbook for Scientist and Engineers*, McGraw-Hill 1965.

McGillem CD, Aunon JI, and Yu K., "Signals and noise in evoked brain potentials," *IEEE Trans. Biomedical Eng.*, 1985, 32: 1012 - 1016.

Mosher JC, Lewis PS, Leahy RM, Singh M, "Multiple dipole modeling of spatio-temporal MEG data," In A.F. Gmitro, et al. (Eds.) *Digital Image Synthesis and Inverse Optics*, San Diego, CA, July 1990, Proc. SPIE 1351:364-375.

Mosher JC, Lewis PS, Leahy RM, "Spatial localization of neural sources using the magnetoencephalogram," *Fifth ASSP Wkshp on Spectrum Estimation and Modeling*, Rochester, NY, Oct 1990:289-293.

Mosher JC, Lewis PS, Leahy RM, "Subspace methods for identifying neural activity from electromagnetic measurements of the brain," *IEEE Proc. 25th Asilomar Conf. on Signals, Systems, and Computers*, Pacific Grove, CA, Nov. 1991:237-241.

Mosher JC, Lewis PS, Lewine J, George J, Leahy RM, Singh M, "Electromagnetic imaging of dynamic brain activity," *Proc. IEEE 1991 Medical Imaging Conf*, Sante Fe, NM, Nov 1991.

Mosher JC, Lewis PS, and Leahy RM, "Multiple dipole modeling and localization from spatio-temporal MEG data," *IEEE Trans. Biomedical Eng*, 1992, 39:541-557.

Oshiro O, Mukai M, Takeuchi F, and Kuriki, S., "Analysis of errors in neuromagnetic localization of multiple current dipole sources," *Phys. Med. Biol.*, 1992, 37:845-852.

Sarvas J, "Basic mathematical and electromagnetic concepts of the biomagnetic inverse problem," *Phys. Med. Biol.*, 1987, 32:11-22.

Sorenson, Harold W. *Parameter Estimation*. New York: Marcel Dekker, 1985.

Snyder AZ, "Dipole source localization in the study of EP generators: a critique," *Electroenceph. clin. Neurophysiol.*, 1991, 80: 321 - 325.

Stoica P, and Nehorai A, "MUSIC, maximum likelihood, and Cramer-Rao Bound," *IEEE Transactions on Acoustics, Speech, and Signal Processing*, 1989, 37:720-741.

Stok CJ, "The influence of model parameters on EEG/MEG single dipole source estimation," *IEEE Trans. Biomedical Eng.*, 1987, 34: 289 - 296.

Therapeutics and Technology Assessment Subcommittee, "Assessment: Magnetoencephalography (MEG)," *Neurology* 1992; 42: 1-4.

Westerkamp JJ, Aunon JI. "Optimum multielectrode a posteriori estimates of single-response evoked potentials," *IEEE Trans. Biomedical Eng.*, 1987, 34: 13 - 22.

Williamson, SJ "MEG versus EEG localization test," Letter to the Editor, *Ann Neruol.* 1991, 30: 222.

Wilson FN, Bayley RH, "The electric field of an eccentric dipole in a homogeneous spherical conducting medium," *Circulation*, 1950, 1:84-92.

Figures:

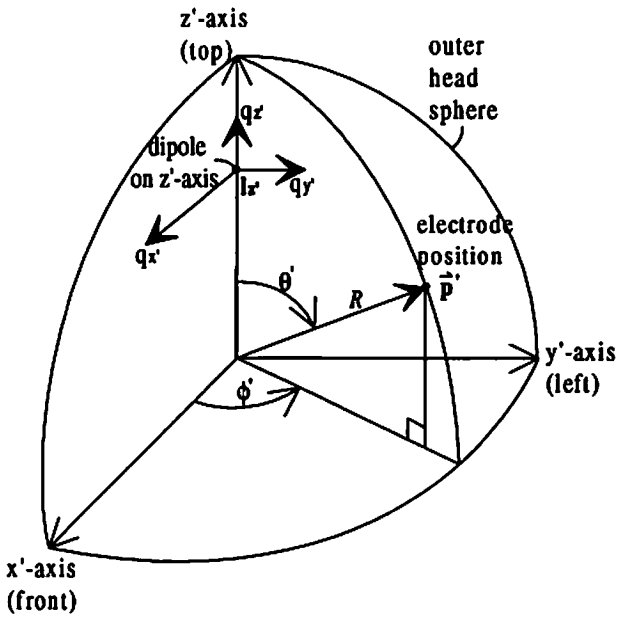

FIGURE 1. EEG Coordinate system for dipole on z-axis in a spherical head model. The EEG model generalizes to arbitrary dipole location using standard coordinate transformations.

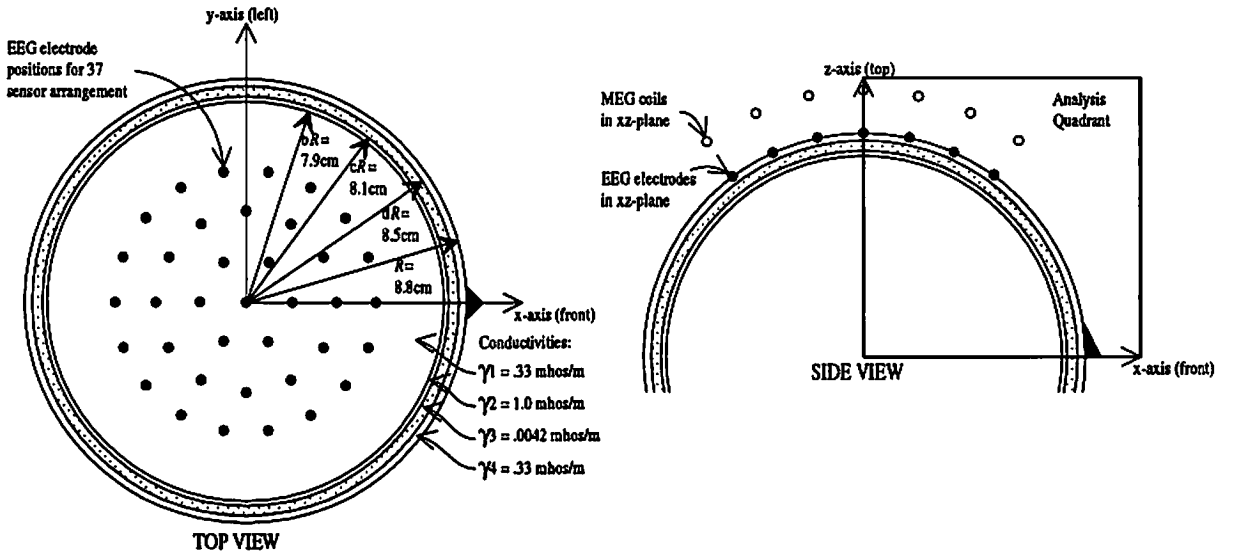

FIGURE 2. Four concentric sphere model of head (Cuffin and Cohen, 1979). The radii and conductivities are shown for the inner brain sphere, the cerebrospinal fluid layer, the skull layer(shaded), and the scalp layer. The EEG electrodes are located on the surface of the scalp at a radius of 8.8 cm; MEG coils are radially oriented 10.5 cm from the head center. For the 37 sensor case, the sensors are positioned in rings of 1, 6, 12, and 18 sensors each, separated by 12 degrees as measured from the z axis. The left figure shows the sensors as viewed from above. The right figure is the side view and shows the EEG electrodes and the MEG coils that lie in the xz-plane (y=0) for the 37 sensor arrangements. The analysis quadrant shows where the CRLB bounds are computed relative to the head spheres and sensors.

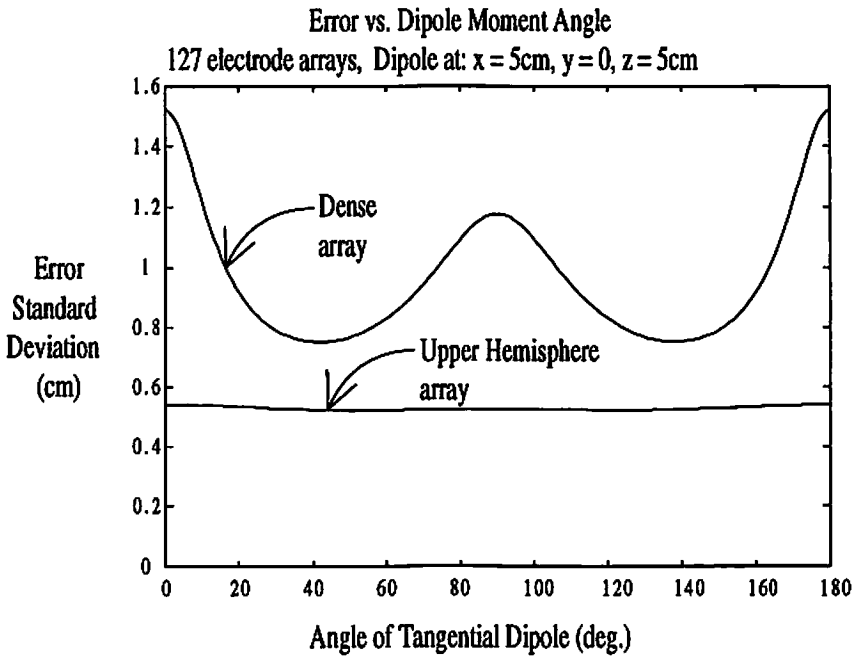

FIGURE 3. RMS Location error as a function of moment orientation angle. The moment direction was restricted to the tangential plane, since radial moments represent blind sources for MEG sensors. For each θ, the RMS location error is calculated using (18). We see here the comparison between two different sensor arrays for the same dipole location. The upper curve is for the dense 127 sensor pattern (see Fig. 9 for description), which is sensitive to the moment orientation, versus the lower curve for the 127 upper hemisphere pattern (Fig. 5), which is insensitive. We retain three values from the curves: the best (lowest) error, the worst, and the average over all θ.

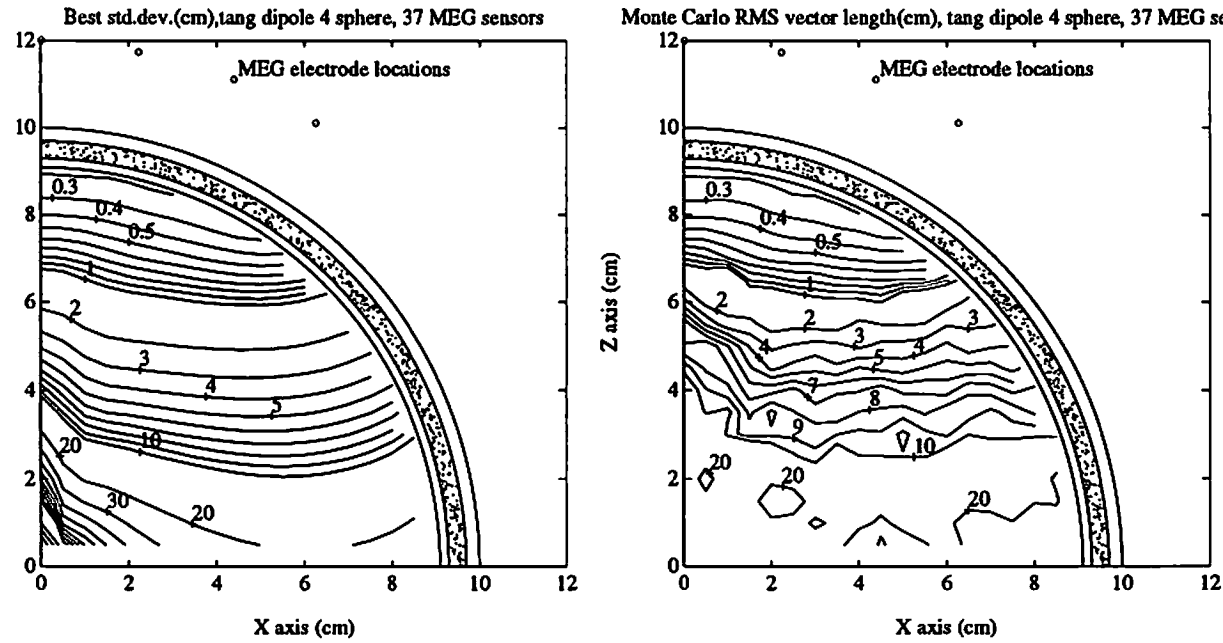

FIGURE 4. Monte Carlo simulation and comparison. The left figure shows the computed CRLBs for a single dipole in a 37 channel MEG system. The right figure is the result of a 100 trial Monte Carlo simulation at each point in a 5 mm grid, using the same dipole intensity and noise variance as the CRLB analysis. The dipole was oriented in the "best" direction, as found from the CRLB analysis. In deep regions, the signal received at the array is much weaker than the additive noise, and the Monte Carlo runs experienced difficulty converging. In the shallow head regions, the signal at the array is improved, and we see excellent agreement between analytic and simulation.

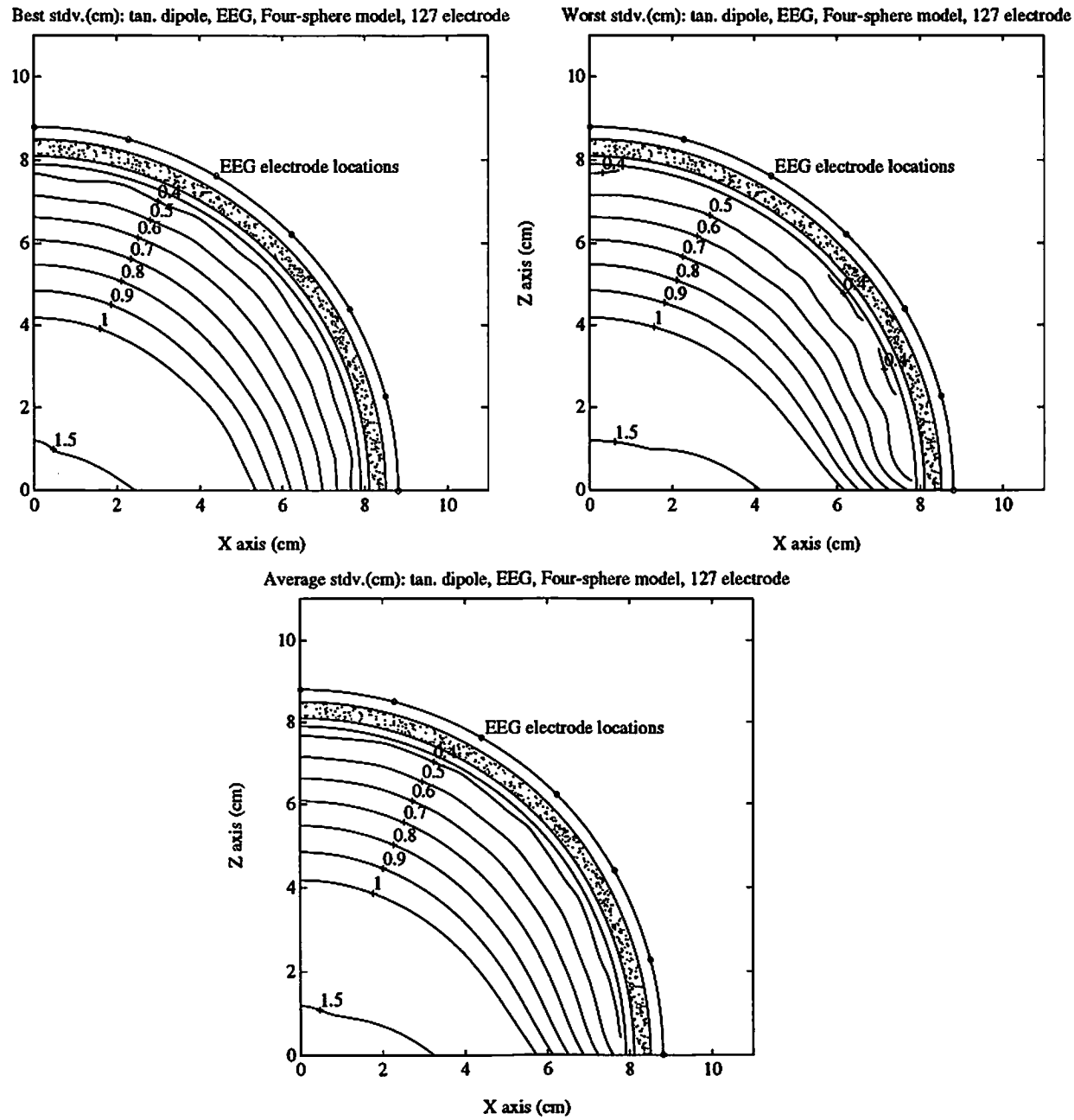

FIGURE 5. EEG Cramer-Rao lower bounds for the 127 upper hemisphere electrode case and a single tangential dipole. The 127 electrode pattern consists of an electrode on the z-axis and six concentric rings separated by 15 degrees consisting of 6, 12, 18, 24, 30, and 36 electrodes per ring, respectively. The contour lines are labeled with the standard deviation of the error (in cm), and a linear scaling factor of $(\sigma_V/Q) = 40$ V/(Am) is assumed, corresponding to a noise standard deviation of 0.4 microvolts and a dipole strength of 10 nanoAmp meters. The tangential dipole is oriented at the angle that (upper left) minimizes the RMS error bound at the given point in the plane and (upper right) maximizes the RMS error bound. The (center) plot shows the average of the error bound calculations for the dipole orientation stepped in one degree increments around a full circle. We emphasize that the curves can be linearly scaled for arbitrary σ_V/Q.

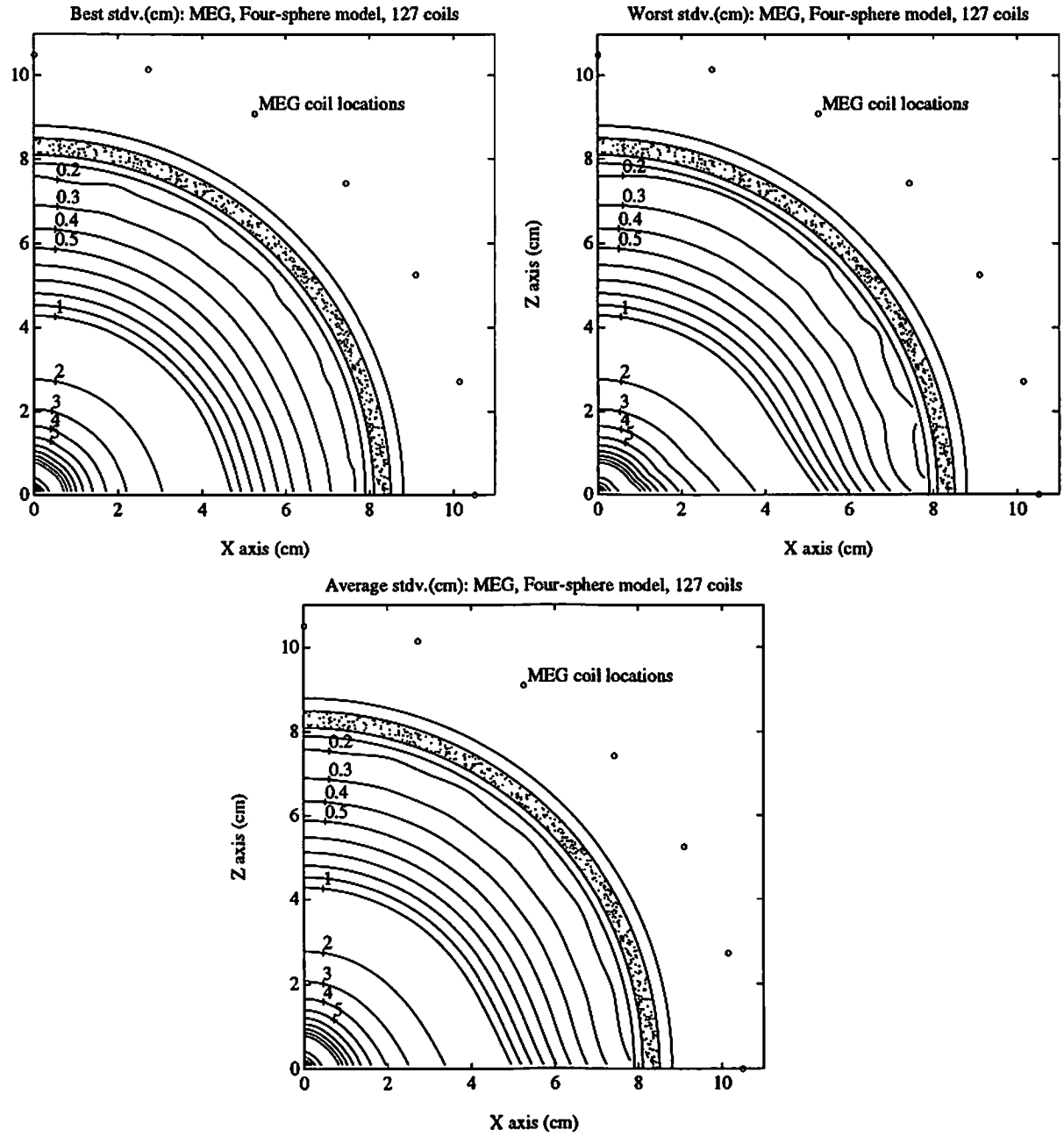

FIGURE 6. MEG Cramer-Rao lower bounds for the 127 upper hemisphere sensor case and a single tangential dipole. A linear scaling factor of $(\sigma_B / Q) = 3.5 \times 10^{-6}$ T/Am is assumed, corresponding to a noise standard deviation of 35 femtoTeslas and a dipole strength of 10 nanoAmp meters. The sensor pattern is identical in angular separation to that of Fig. 5 and the sensors are 10.5 cm from the head origin. The best, worst, and average moment orientations are again presented in the upper left, right, and center plots, respectively. Both the EEG and MEG results show little sensitivity to moment orientation for this pattern and single dipole. We emphasize that the curves can be linearly scaled for arbitrary σ_B/Q.

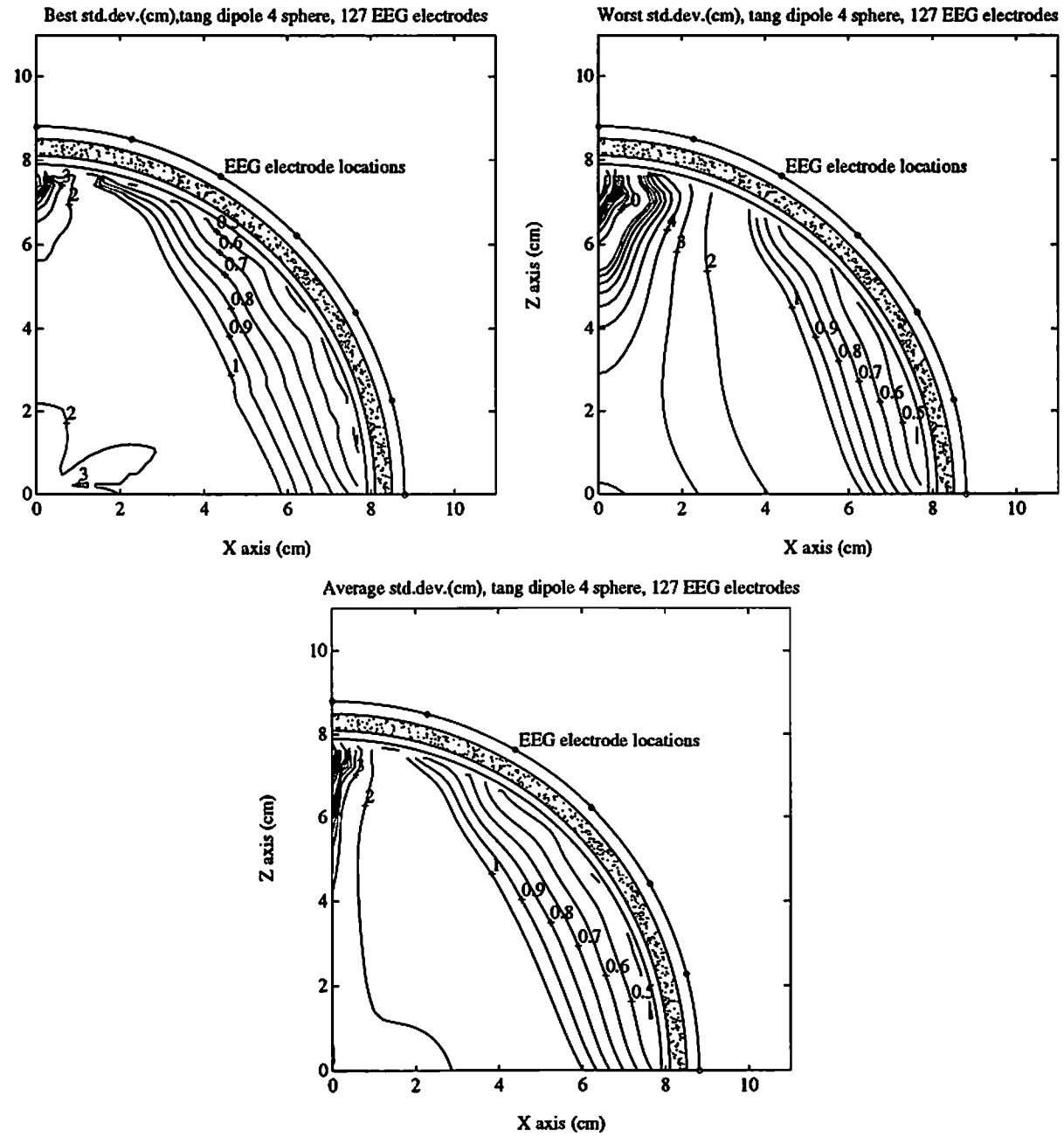

FIGURE 7. EEG Cramer-Rao lower bounds for the 127 upper hemisphere electrode case and two tangential dipoles. The sensor pattern is identical to that of Fig. 5. The first dipole is at any given point in the positive x-z plane and the second is located on the z-axis at 7.5 cm. The contour level (in cm) is the RMS error bound of the first dipole due to the presence of the second dipole. As in the other examples, a linear scaling factor of $(\sigma_V / Q) = 40$ V/(Am) is assumed. The best, worst, and average moment orientation pairs are again presented in the upper left, right, and center plots, respectively. Compared with Fig. 5, we observe the strong dependence on dipole orientation between two dipoles.

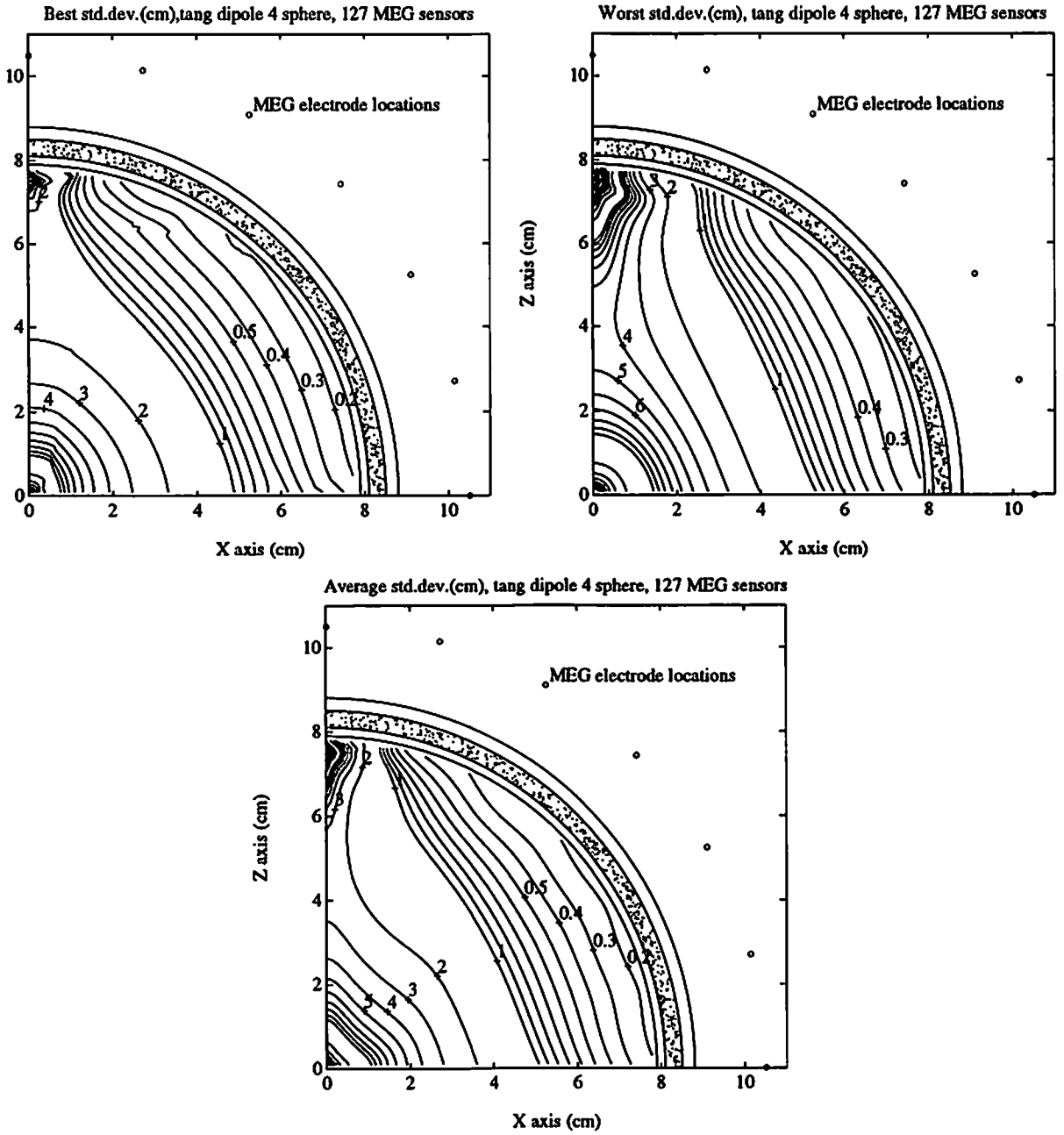

FIGURE 8. MEG Cramer-Rao lower bounds for the 127 sensor upper hemisphere case and two tangential dipoles. The sensor pattern is identical to that of Fig. 6, and the analysis procedure is identical to that of Fig. 7. As in the other MEG examples, a linear scaling factor of $(\sigma_B/Q) = 3.5\times10^{-6}$ T/Am is assumed. The best, worst, and average moment orientation pairs are again presented in the upper left, right, and center plots, respectively.

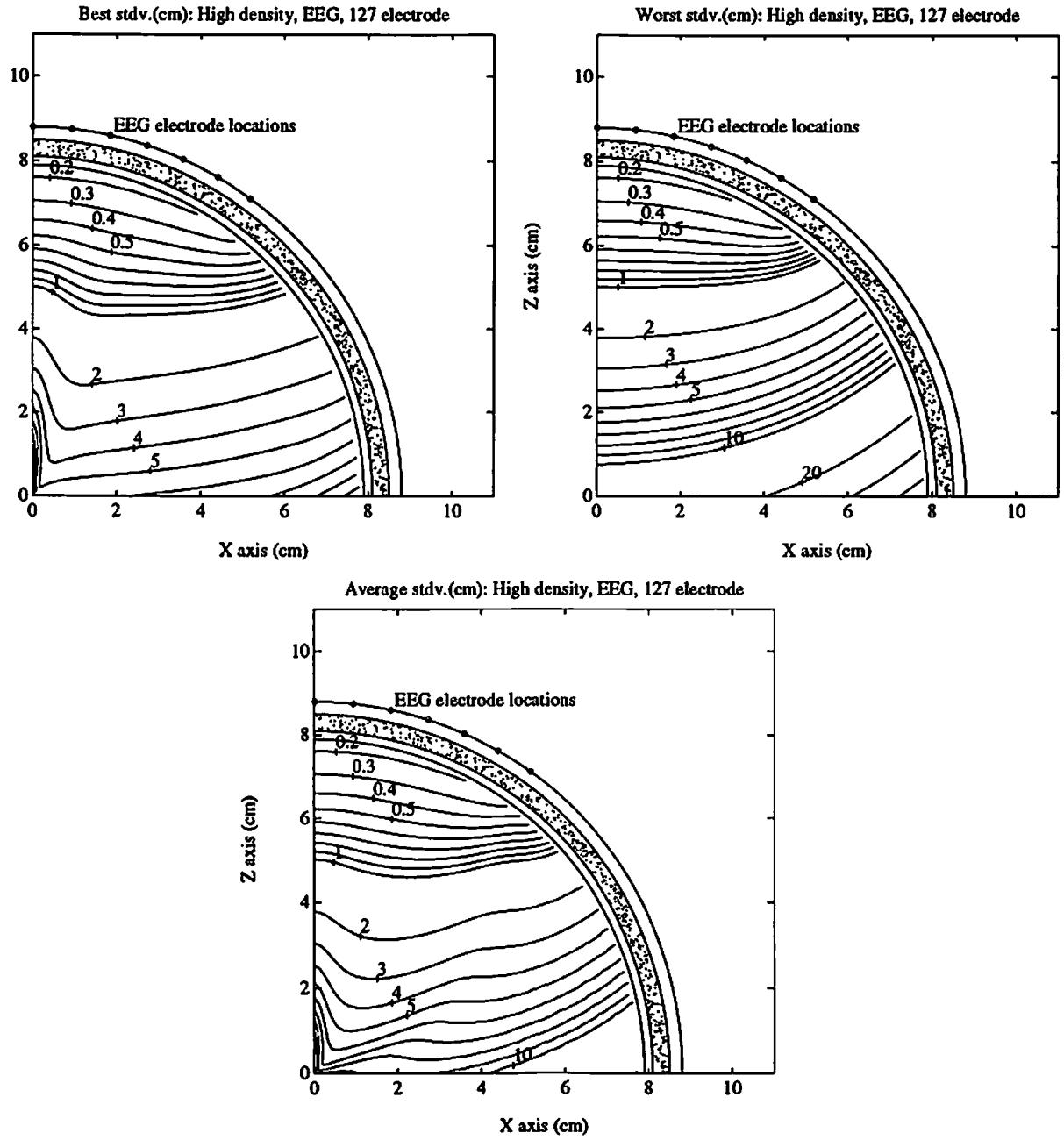

FIGURE 9. EEG Cramer-Rao lower bounds for the dense 127 electrode case and a single tangential dipole at any given point in the positive x-z plane. The array pattern is constructed as in Fig. 5 for the 127 sensor upper hemisphere pattern, but now separated by 6 degrees, instead of 15 degrees. As in the other EEG examples, a linear scaling factor of $(\sigma_V/Q) = 40$ V/(Am) is assumed. The best, worst, and average moment orientations are again presented in the upper left, right, and center plots, respectively.

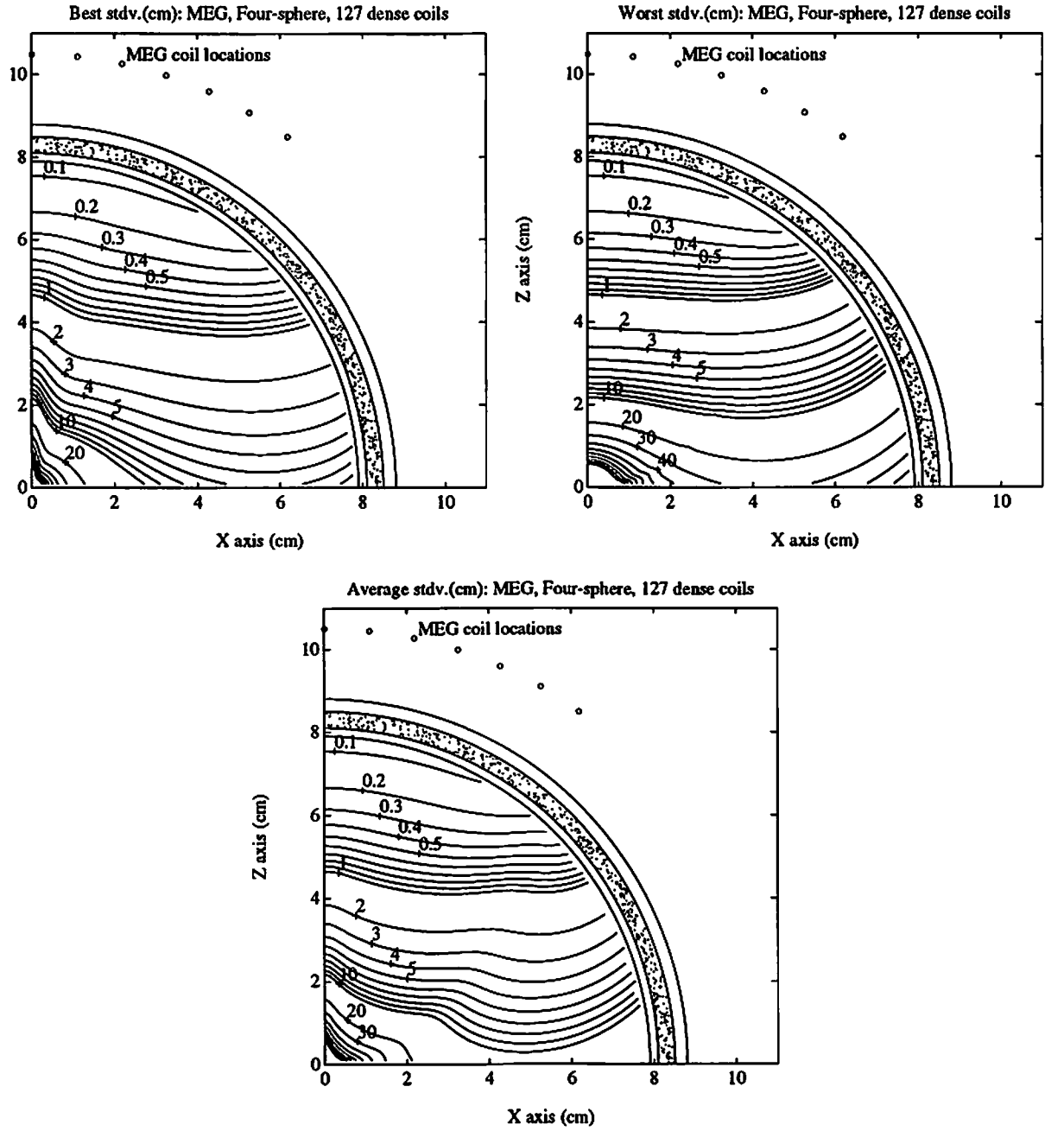

FIGURE 10. MEG Cramer-Rao lower bounds for the dense 127 sensor case and a single tangential dipole at any given point in the positive x-z plane. The 127 sensors are arranged in the same angular pattern as in Fig. 9, except that they are located 10.5 cm from the head origin. As in the other MEG examples, a linear scaling factor of $(\sigma_B/Q) = 3.5\times10^{-6}$ T/Am is assumed. The best, worst, and average moment orientations are again presented in the upper left, right, and center plots, respectively.

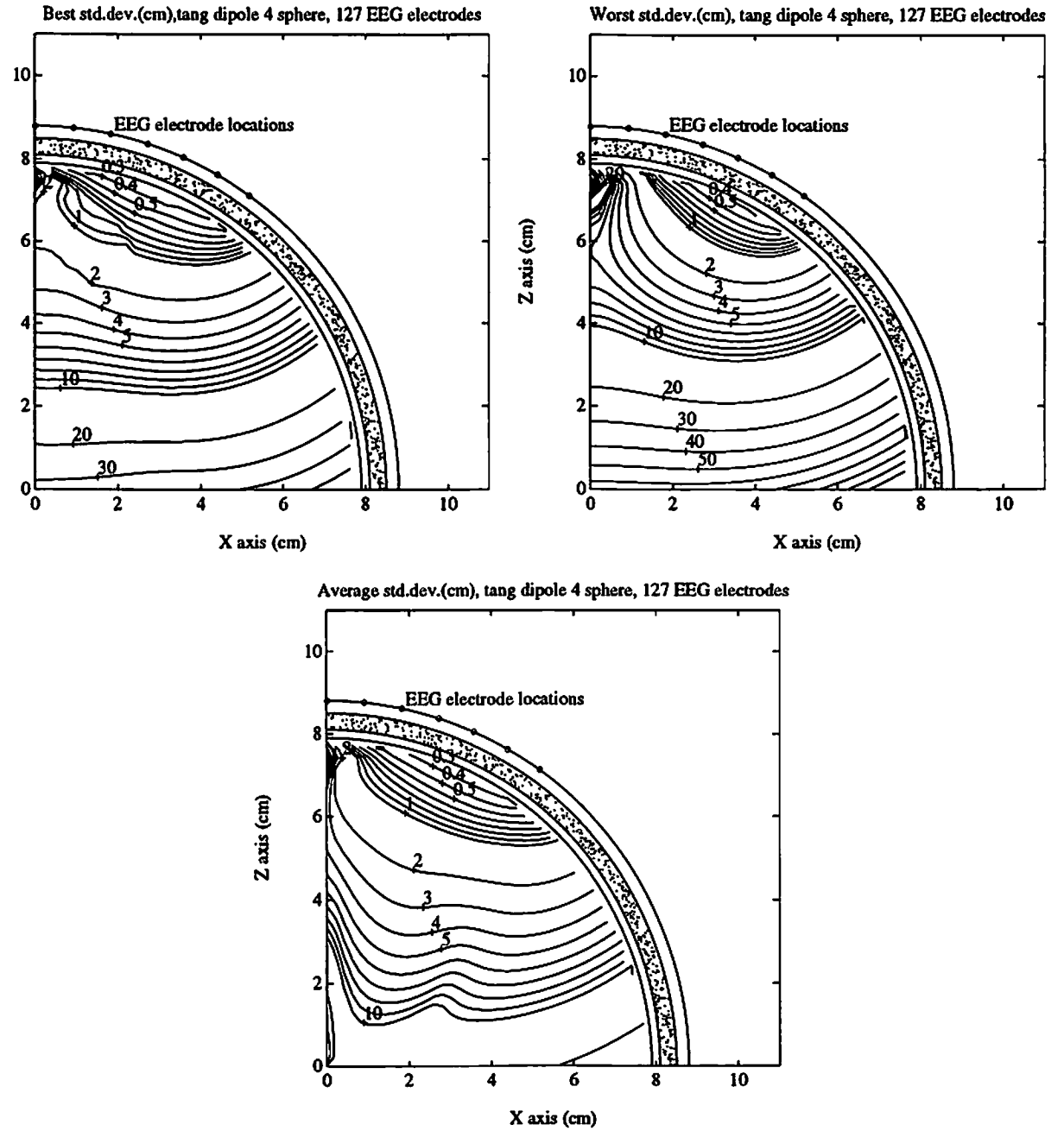

FIGURE 11. EEG Cramer-Rao lower bounds for the dense 127 electrode case and two tangential dipoles. The sensor pattern is identical to that of Fig. 9. The first dipole is at any given point in the positive x-z plane and the second is located on the z-axis at 7.5 cm. The contour level (in cm) is the RMS error bound of the first dipole due to the presence of the second dipole. As in the other examples, a linear scaling factor of $(\sigma_v/Q) = 40$ V/(Am) is assumed. The best, worst, and average moment orientations are again presented in the upper left, right, and center plots, respectively.

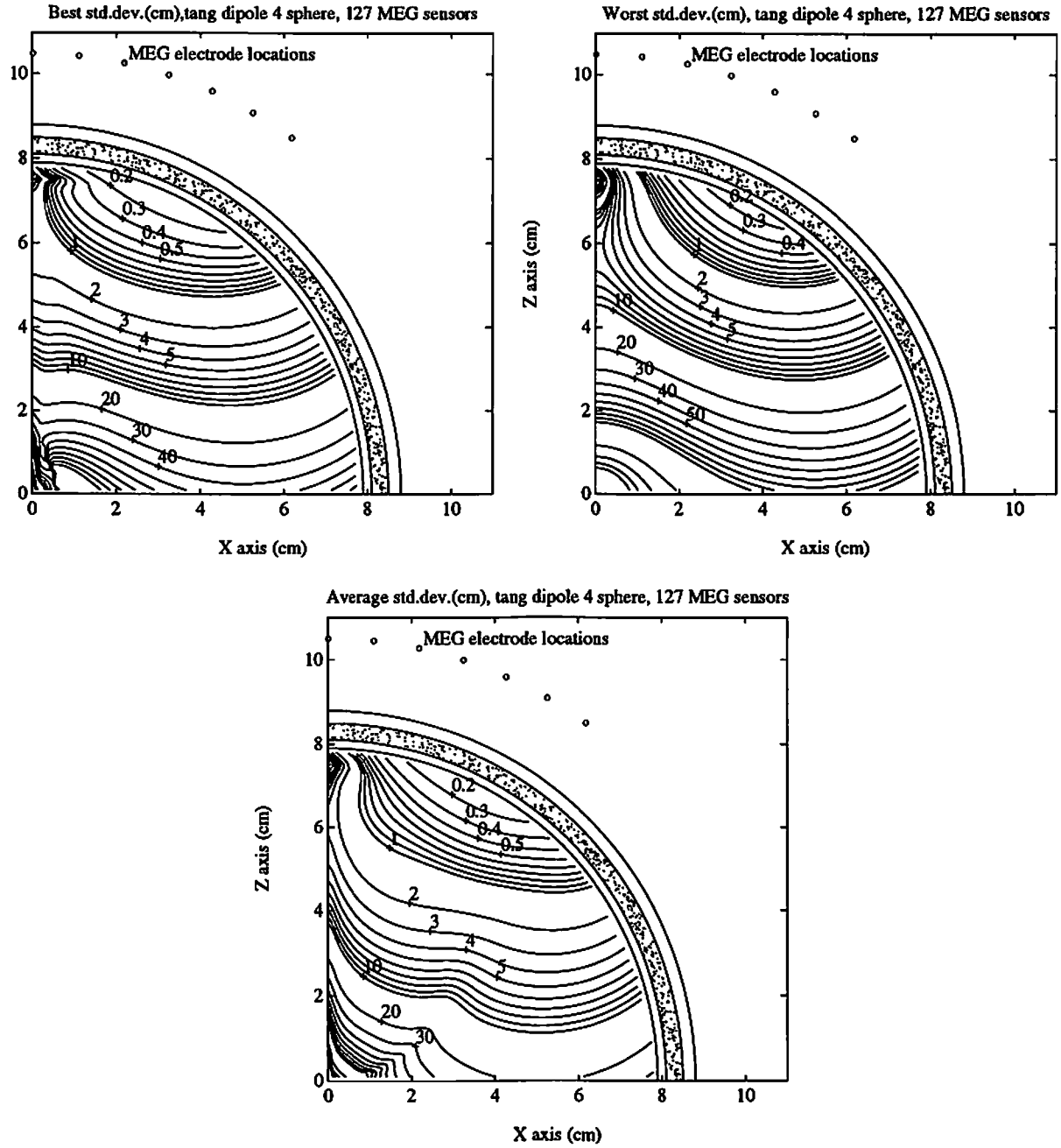

FIGURE 12. MEG Cramer-Rao lower bounds for the dense 127 sensor case and two tangential dipoles. The sensor pattern is identical to that of Fig. 10. As in the other MEG examples, a linear scaling factor of $(\sigma_B/Q) = 3.5\times10^{-6}$ T/Am is assumed. The best, worst, and average moment orientations are again presented in the upper left, right, and center plots, respectively.

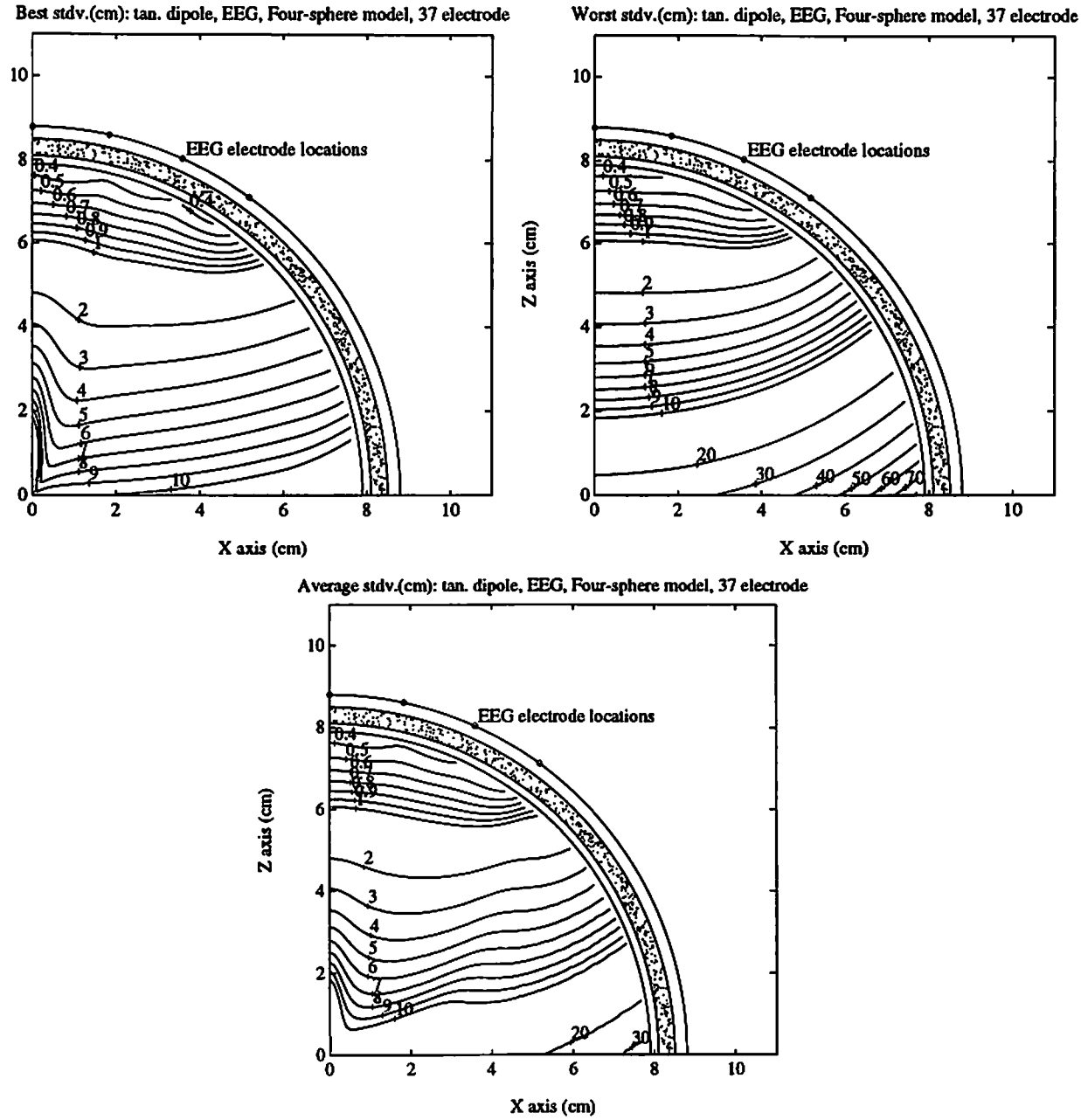

FIGURE 13. EEG Cramer-Rao lower bounds for the 37 electrode case and a single tangential dipole at any given point in the positive x-z plane. The 37 electrode pattern is described and displayed in Fig. 2 and is similar to commercially available MEG instruments. As in the other EEG examples, a linear scaling factor of $(\sigma_V/Q) = 40$ V/(Am) is assumed. The best, worst, and average moment orientations are again presented in the upper left, right, and center plots, respectively.

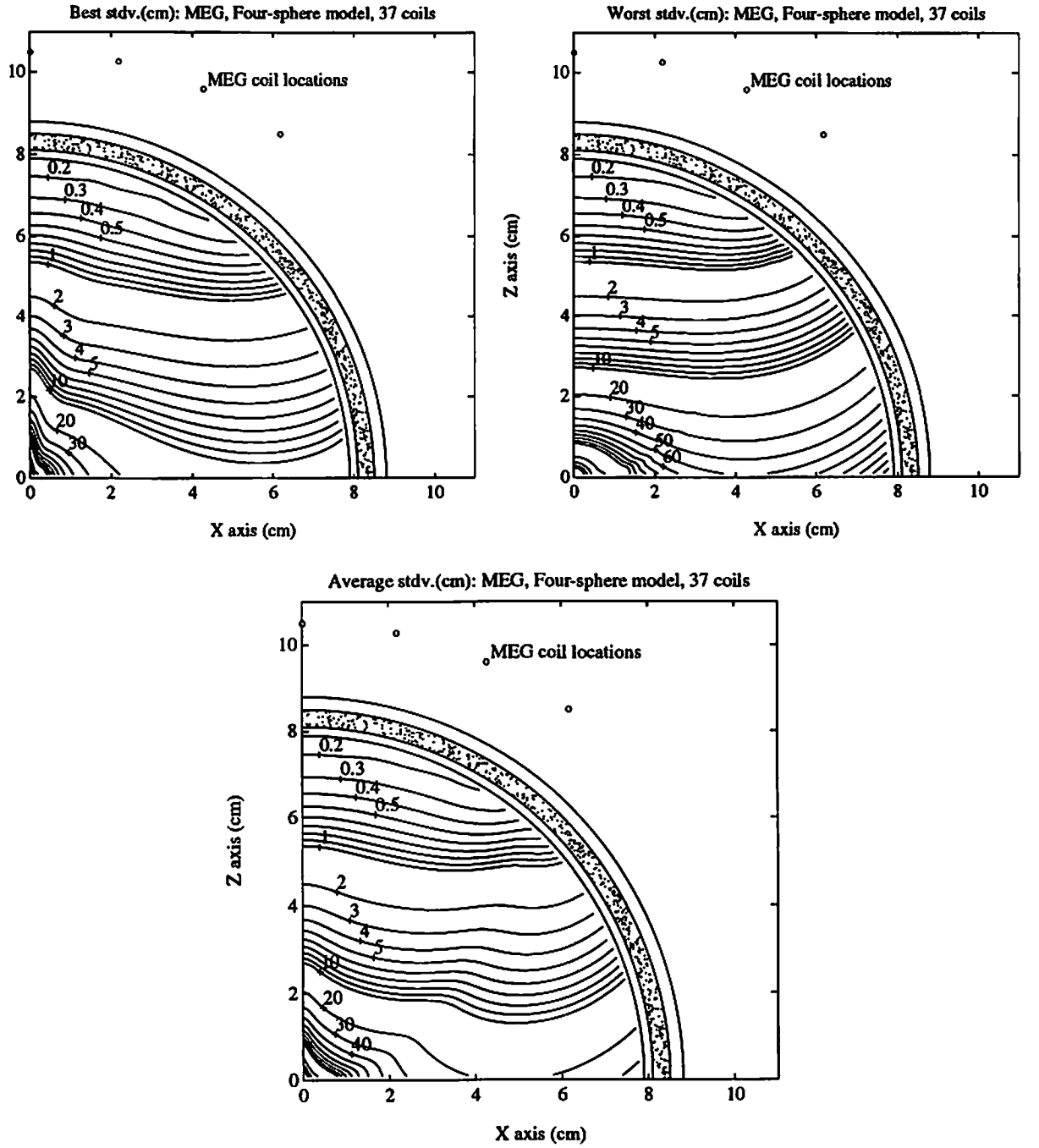

FIGURE 14. MEG Cramer-Rao lower bounds for the 37 coil case and a single tangential dipole at any given point in the positive x-z plane. The sensor pattern is identical in angular separation to that of Fig. 13 and the sensors are again 10.5 cm from the head origin. As in the other MEG examples, a linear scaling factor of $(\sigma_B / Q) = 3.5 \times 10^{-6}$ T/Am is assumed. The best, worst, and average moment orientations are again presented in the upper left, right, and center plots, respectively.

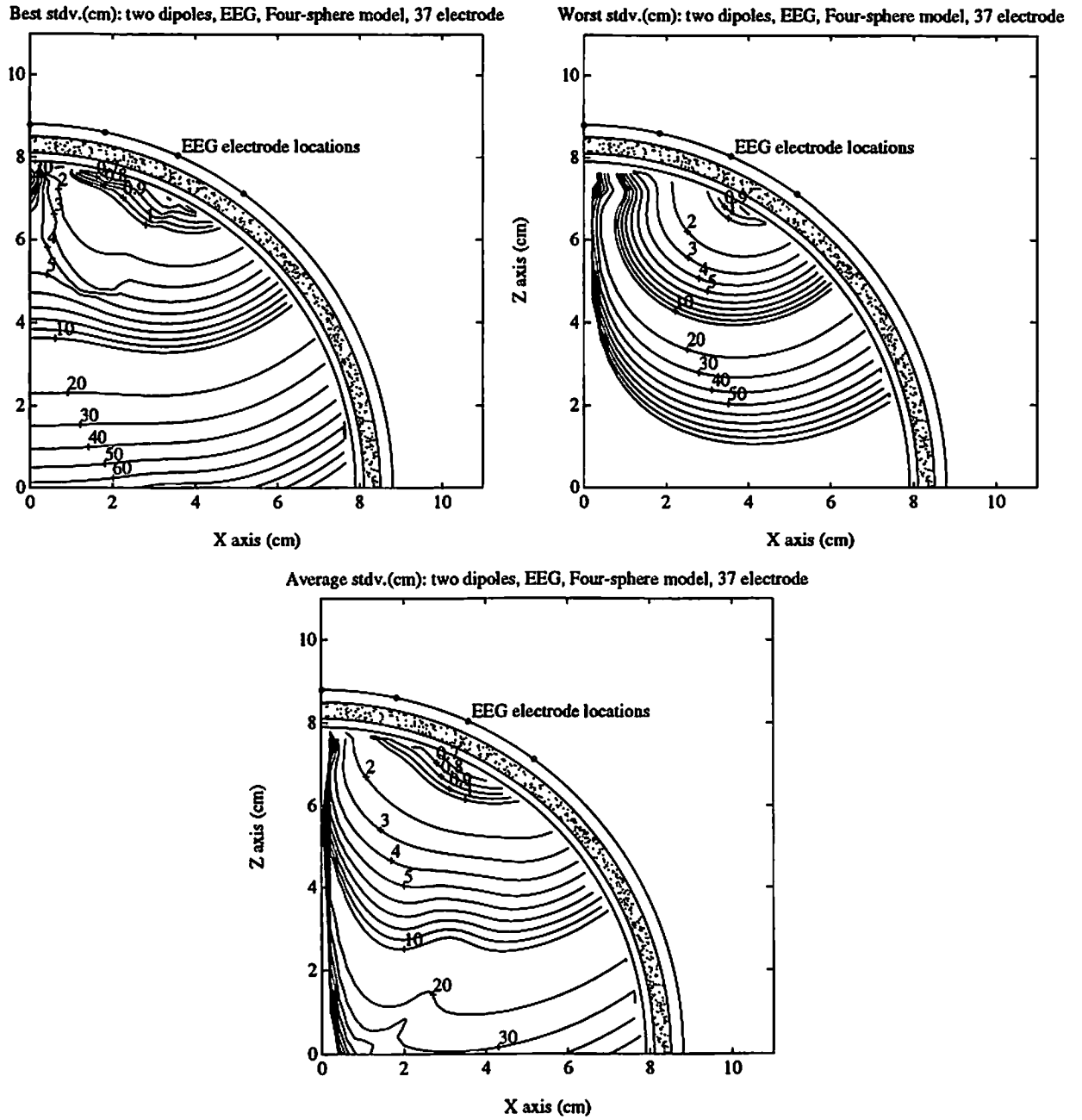

FIGURE 15. EEG Cramer-Rao lower bounds for the 37 electrode case and two tangential dipoles. The first dipole is at any given point in the positive x-z plane and the second is located on the z-axis at 7.5 cm. The contour level (in cm) is the RMS error bound of the first dipole due to the presence of the second dipole. As in the other EEG examples, a linear scaling factor of $(\sigma_V/Q) = 40$ V/(Am) is assumed. The best, worst, and average moment orientations are again presented in the upper left, right, and center plots, respectively.

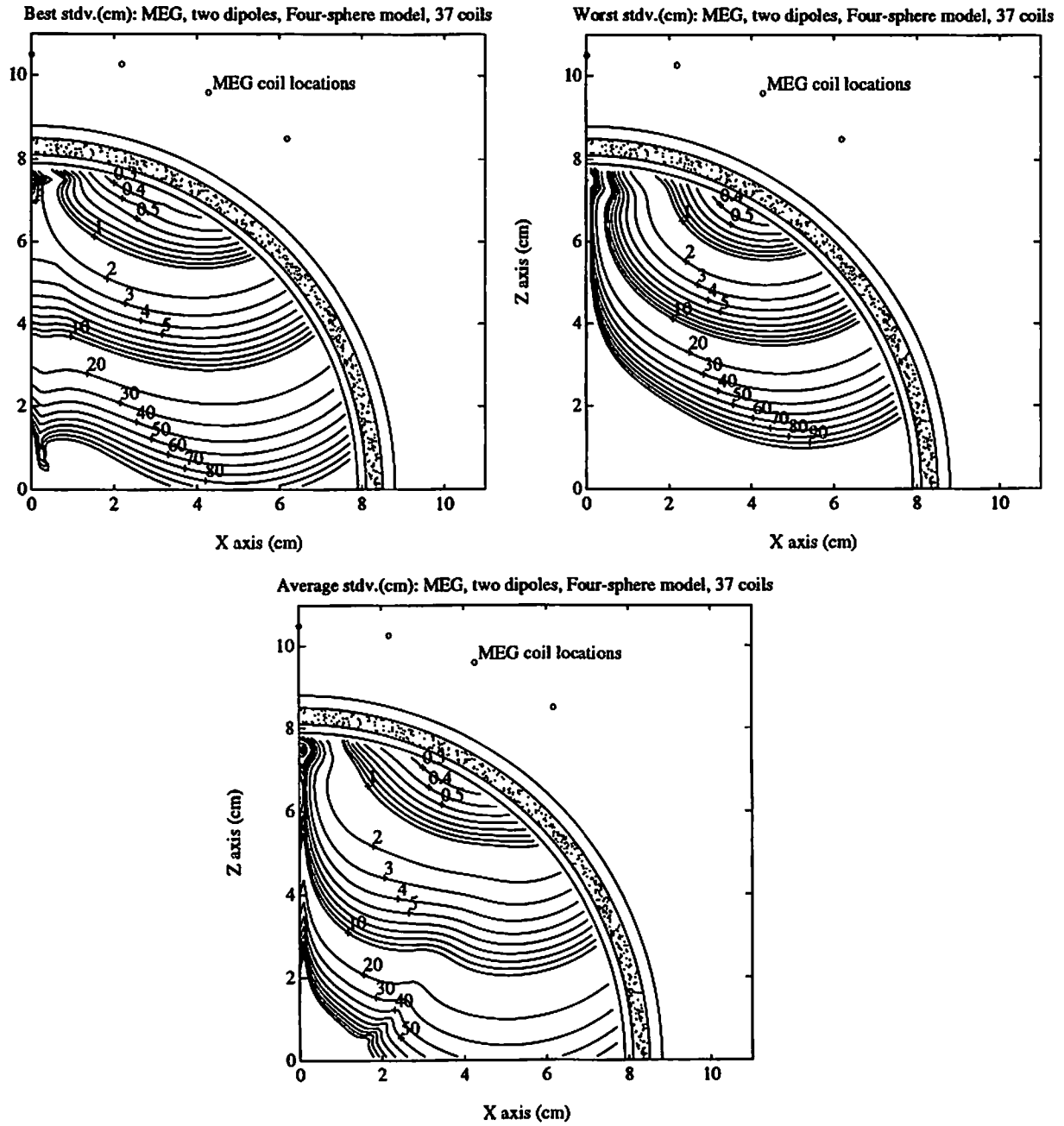

FIGURE 16. MEG Cramer-Rao lower bounds for the 37 coil case and two tangential dipoles. The sensor arrangement is identical to that of Fig. 14. As in other MEG examples, a linear scaling factor of $(\sigma_B/Q) = 3.5\times10^{-6}$ T/Am is assumed. The best, worst, and average moment orientations are again presented in the upper left, right, and center plots, respectively.

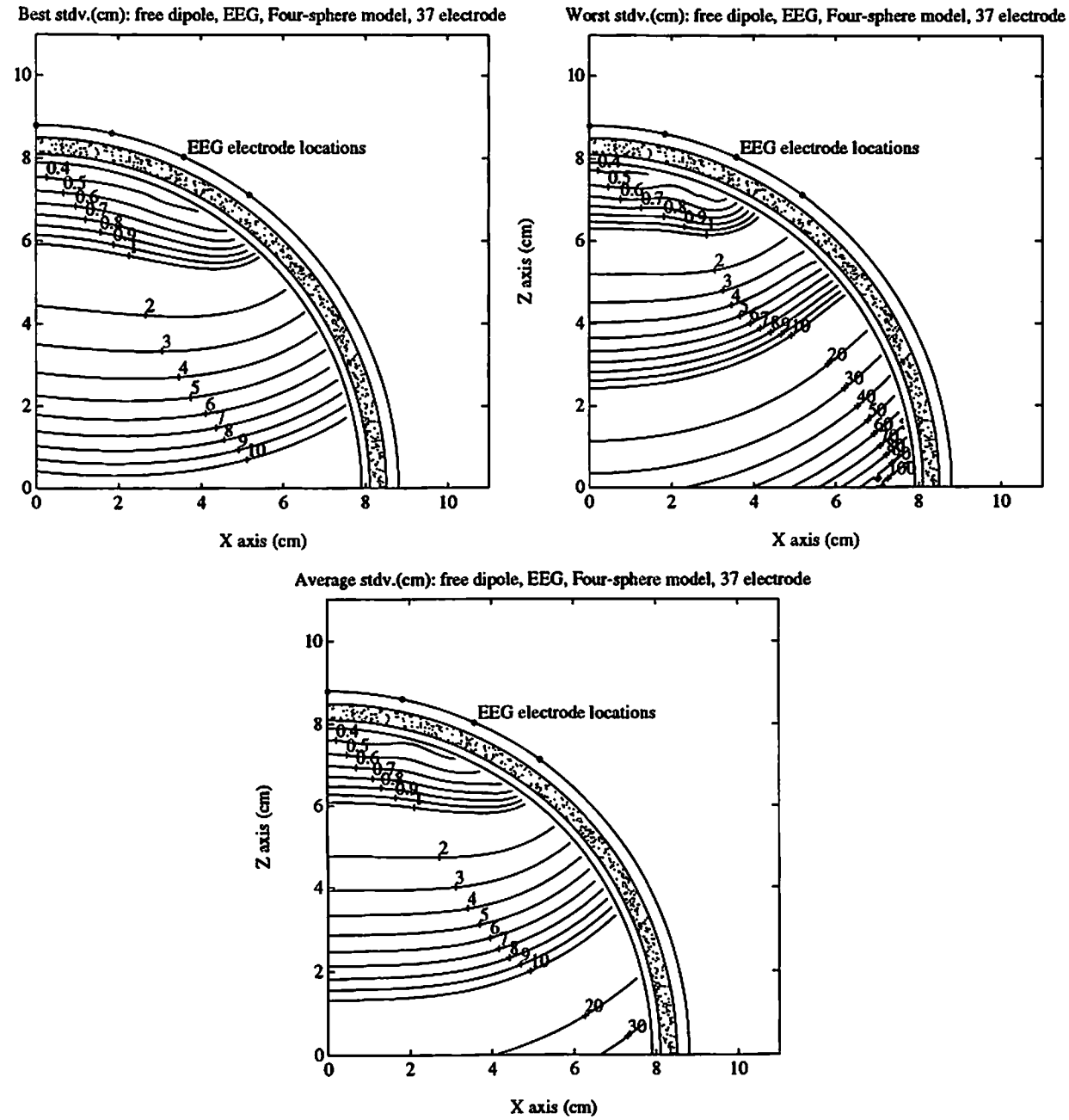

FIGURE 17. EEG Cramer-Rao lower bounds for the 37 electrode case and a single freely oriented dipole (the dipole can have tangential and radial components) at any given point in the positive x-z plane. As in the other EEG examples, a linear scaling factor of $(\sigma_v/Q) = 40$ V/(Am) is assumed. The best, worst, and average moment orientations are again presented in the upper left, right, and center plots, respectively.

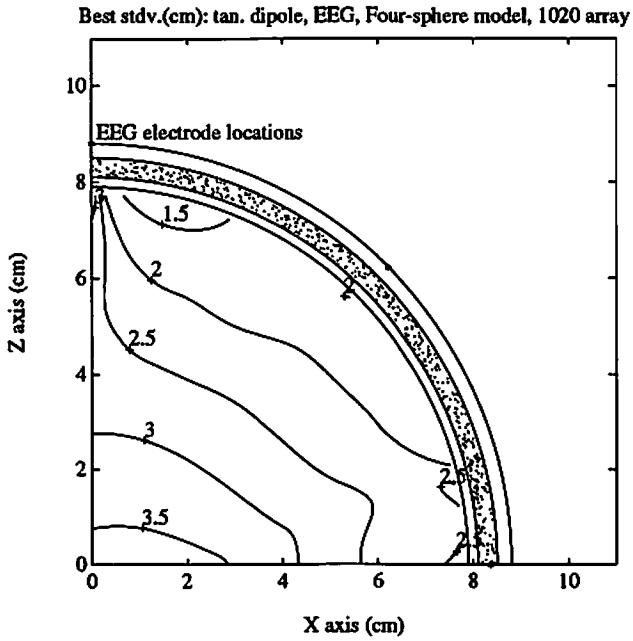

FIGURE 18. EEG Cramer-Rao lower bounds for the 21 electrode arrangement of the standard Ten-Twenty arrangement and a single tangential dipole at any given point in the positive x-z plane. The contour lines are labeled with the RMS error bounds (in cm), and a linear scaling factor of $(\sigma_v/Q) = 40$ V/(Am) is again assumed. The tangential dipole is oriented at the angle that minimizes the error bound at the given point in the plane.

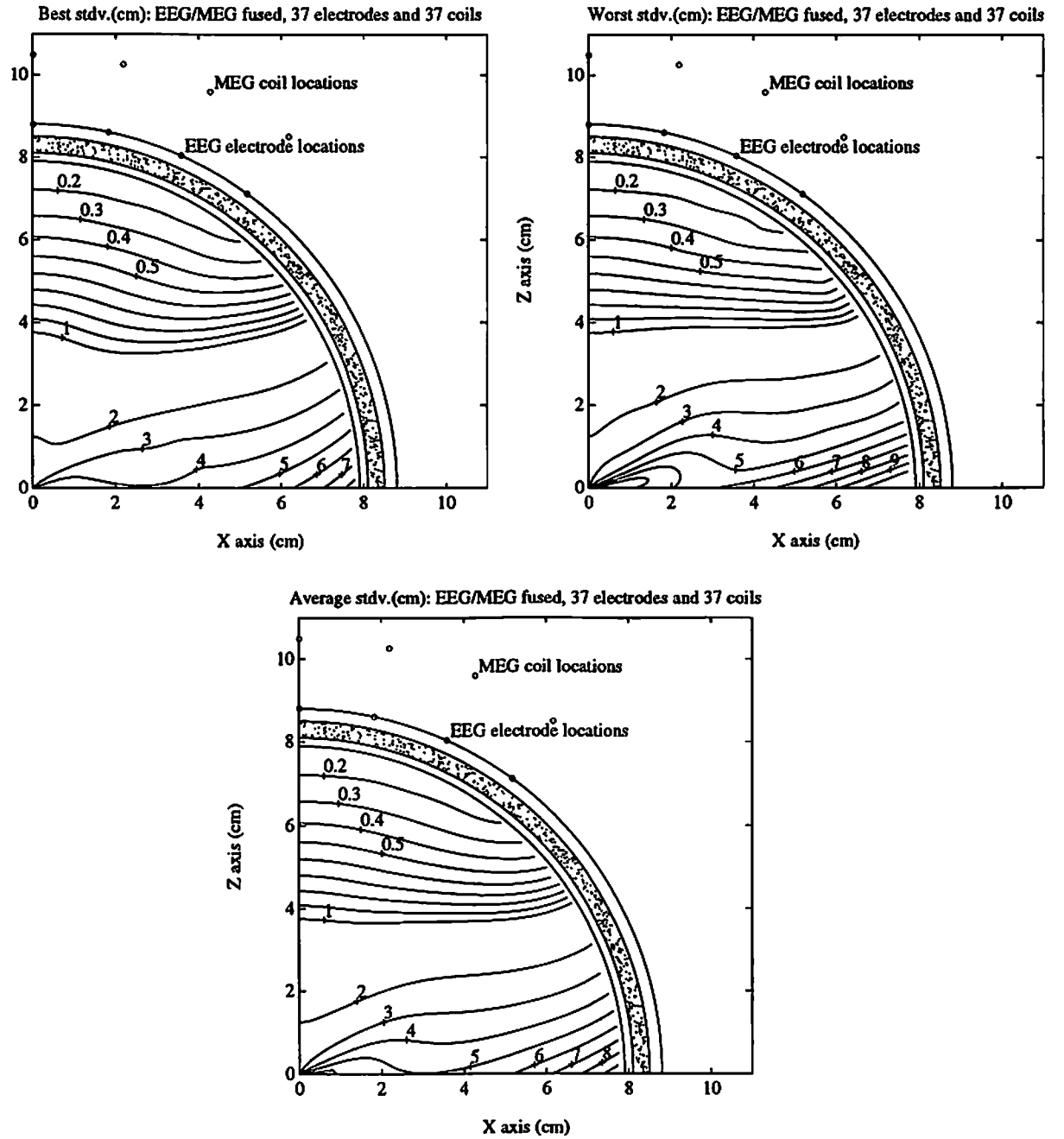

FIGURE 19. Combined EEG/MEG Cramer-Rao lower bounds for the 37 electrode and 37 magnetic sensor array and a single tangential dipole at any given point in the positive x-z plane. As in the other studies, $(\sigma_V/Q) = 40$ V/(Am), ($(\sigma_B/Q) = 3.5\times10^{-6}$ T/Am) ; however unlike all other results presented in this paper, these results do *not* scale linearly with other considerations of noise and dipole intensity. The best, worst, and average moment orientations are again presented in the upper left, right, and center plots, respectively.